Chapter 2

Solar Wind Turbulence

This chapter introduces such concepts from turbulence theory that are relevant for scattering theories used in the study of cosmic-ray modulation. The depth of the subject allows little room for more than an introductory treatment. For a more thorough treatment of the topics covered in this chapter, the interested reader should consult the given references.

A general introduction to the underlying ideas behind concepts such as the power spectrum will be given, followed by more specific treatments of turbulence in the solar wind. Such spacecraft observations as are relevant to the modelling of turbulence power spectra will be discussed, and the spectral forms assumed in this study will be described in detail.

2.1 General Background on the Turbulence Power Spectrum

The power spectrum of the fluctuations of the turbulent heliospheric magnetic field is a key input for the scattering theories used to derive cosmic-ray diffusion coefficients, and hence is integral to the understanding of cosmic-ray modulation. A brief introduction to the mathematical concepts underlying such a spectrum is now presented.

As a point of departure, a Reynolds decomposition of the total heliospheric magnetic field (HMF) vector $\mathbf{B}$ is made, so that it is assumed to be the sum of some uniform (on large temporal scales) component $\mathbf{B}_o$, such as the Parker field, and a fluctuating component $\mathbf{b}$,

$$\mathbf{B} = \mathbf{B}_o + \mathbf{b}, \tag{2.1}$$

so that $\langle \mathbf{B} \rangle = \mathbf{B}_o$ and $\langle \mathbf{b} \rangle = 0$, where the brackets denote a suitable average. The solar wind velocity vector can be similarly decomposed, as can the solar wind density. However, throughout what follows, the assumption of a locally incompressible solar wind flow is made, in that the solar wind density is assumed to vary on temporal scales much larger than those relevant to the averaging processes implicit to the turbulent effects of interest to this study [see, *e.g.*, *Breech*, 2008].

A function can be defined to give a measure of the correlation of the fluctuations between two points. Such a correlation tensor, if it were solely a function of spatial separation, in turn

implying the assumption of homogeneous turbulence, can be represented as [see, *e.g.*, *Batchelor*, 1970; *Tennekes and Lumley*, 1972; *Davidson*, 2004; *Matthaeus et al.*, 2007]

$$R_{ij}\left(\mathbf{r}\right) = \left\langle \mathbf{b}_i(\mathbf{x})\mathbf{b}_j(\mathbf{x}+\mathbf{r})\right\rangle, \tag{2.2}$$

where the applicable quantities are the magnetic field fluctuations $\mathbf{b}(\mathbf{x})$ and $\mathbf{b}(\mathbf{x}+\mathbf{r})$, a distance $\mathbf{r}$ apart, and angle brackets denoting an ensemble average. Note that the assumption of spatially homogeneous turbulence implies that the correlation function is not a function of $\mathbf{x}$ [*Bieber et al.*, 1996] and that $R_{ij}\left(\mathbf{r}\right) = R_{ji}\left(-\mathbf{r}\right)$ [*Matthaeus et al.*, 2007]. Furthermore, the divergence free nature of magnetic field fluctuations implies that

$$\frac{dR_{ij}\left(\mathbf{r}\right)}{dx_i} = 0. \tag{2.3}$$

Note also that, when the correlation function is evaluated at zero separation, $R_{ii}(0) = \delta B_i^2$, with δB_i^2 the mean square amplitude of the i-th fluctuating component.

The homogeneous symmetric spectral tensor, given by [*Batchelor*, 1970],

$$S_{ij}\left(\mathbf{k}\right) = \left(\delta_{ij} - \frac{k_i k_j}{k^2}\right) S\left(\mathbf{k}\right), \tag{2.4}$$

with $S\left(\mathbf{k}\right)$ the modal spectral density and δ_{ij} the Kronecker symbol, can be obtained from a Fourier transform of the correlation functions

$$S_{ij}\left(\mathbf{k}\right) = \frac{1}{\left(2\pi\right)^3}\int d^3r R_{ij}\left(\mathbf{r}\right)\exp\left(-i\mathbf{k}\cdot\mathbf{r}\right). \tag{2.5}$$

Taking the inverse Fourier transform,

$$R_{ij}\left(\mathbf{r}\right) = \int d\mathbf{k} S_{ij}\left(\mathbf{k}\right)\exp\left(i\mathbf{k}\cdot\mathbf{r}\right), \tag{2.6}$$

it follows from Equation 2.3 that

$$\int d\mathbf{k} k_i S_{ij}\left(\mathbf{k}\right)\exp\left(i\mathbf{k}\cdot\mathbf{r}\right) = 0. \tag{2.7}$$

This holds for all k-space, hence

$$k_i S_{ij} = 0. \tag{2.8}$$

The physical significance of the modal power spectrum is as follows: if $\mathbf{b}\left(\mathbf{k}\right)$ were the Fourier transform of $\mathbf{b}\left(\mathbf{x}\right)$, the omnidirectional power spectrum $E\left(k\right)$ would be a measure of the energy in the k-th mode of the fluctuation $\mathbf{b}\left(\mathbf{k}\right)$ [*Davidson*, 2004], and is related to the mean square amplitude of the fluctuations by

$$\int_{-\infty}^{\infty} d^3k S_{ij}\left(\mathbf{k}\right) = \left\langle b^2\right\rangle \equiv \delta B^2. \tag{2.9}$$

The spectrum itself represents a cascade of energy from large scales to smaller scales [see, *e.g.*, *Batchelor*, 1970; *Tennekes and Lumley*, 1972; *Zhou et al.*, 2004], and when its wavenumber dependence is considered, several subranges can be defined, depending on the processes driving the

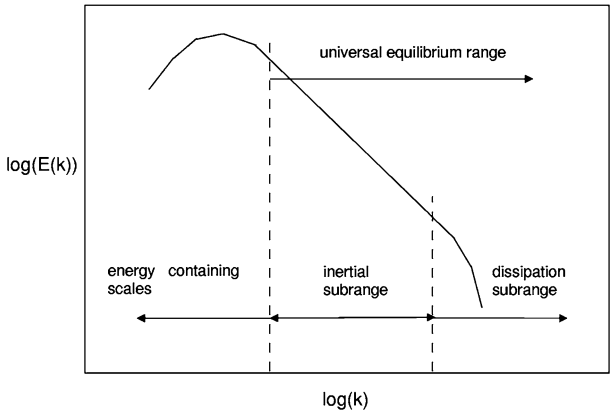

Figure 2.1: Generic depiction of the wavenumber dependence of the omnidirectional power spectrum of fully developed turbulence, indicating various subranges [*Petrosyan et al.*, 2010].

turbulence, and the interactions themselves. Fig. 2.1 illustrates these subranges. At the lowest wavenumbers, an energy range occurs, representing scales at which energy is added to the spectrum, driving the turbulent eddies, and providing the source of energy for the turbulent cascade [*Goldstein et al.*, 1995a]. The universal equilibrium subrange begins beyond a certain lengthscale, hereafter referred to in this study as the turnover scale, and is characterized, according to the theory of universal equilibrium [*Kolmogorov*, 1941], by eddies that are both statistically isotropic, and in statistical equilibrium with one another [*Batchelor*, 1970; *Davidson*, 2004]. This subrange is divided into the inertial subrange, where energy transfer is dominated by inertial forces between the fluctuations [*Batchelor*, 1970], and the steeper dissipation range, where the energy injected at the energy range, after having cascaded down through the scales corresponding to the inertial range, is removed from the spectrum, ultimately heating the background plasma [*Smith et al.*, 1990; *Goldstein et al.*, 1995a; *Leamon et al.*, 1998a]. Note, however, that the energy does not necessarily cascade only from larger to smaller scales. *Dmitruk and Matthaeus* [2007] showed by means of numerical turbulence simulations that wavemodes in the energy range of the spectrum can acquire energy from shorter wavelength modes due to an inverse cascade of energy. Possible subranges within the inertial range [see, *e.g.*, *Wicks et al.*, 2011] are not considered in this study.

The above discussion of the inertial range followed the theory of *Kolmogorov* [1941], which from dimensional analysis predicted a spectral index of $-5/3$ for the inertial range, as indicated in Fig. 2.1. However, this analysis assumes fully developed turbulence in an isotropic, homogeneous fluid, and that the energy cascade flows directly from larger eddies to smaller ones only. If a magnetized fluid were considered, things become more complicated, as the effect of long range forces need to be taken account of [*Petrosyan et al.*, 2010]. *Iroshnikov* [1963] and *Kraichnan* [1965], assuming isotropic, homogeneous turbulence in the presence of a uniform magnetic field, found the spectral index of the inertial range to have a value of $-3/2$, also by means of dimensional analysis.

The spectral index of the dissipation range is expected to be steeper than that of the inertial

range, and dependent on the processes driving the ultimate dissipation of energy [*Smith et al.*, 1990]. From magnetohydrodynamic theory, the spectral index of the dissipation range is expected to be equal to -3, or steeper, as any other value would imply that the mean square of the curl of the total magnetic field would be divergent [*Bieber et al.*, 1988; *Smith et al.*, 1990; *Bieber et al.*, 1994]. The solar wind, however, is a weakly collisional plasma, and thus the dissipation of energy below scales at which magnetohydrodynamic theory no longer applies must of necessity be described by kinetic [see, *e.g.*, *Marsch*, 2006] or gyrokinetic theories [see, *e.g.*, *Howes et al.*, 2008].

As indicated above, the presence of turbulence in an MHD fluid leads to scenarios more complicated than those envisaged by models of purely hydrodynamic turbulence [see, *e.g.*, *Davidson*, 2004; *Zhou et al.*, 2004]. Various models for the treatment of turbulence and the power spectra for the specific case of the solar wind will be discussed in some detail in the next section.

2.2 Turbulence Models

Shebalin et al. [1983], in an analysis of simulated 2D magnetohydrodynamic turbulence in the presence of a uniform external magnetic field, found that initially isotropic (in wavenumber space) turbulent states evolved into anisotropic ones. Extending the abovementioned study to three dimensions, *Oughton et al.* [1994] confirmed the results of *Shebalin et al.* [1983], and furthermore found that excitations were preferentially transferred to modes with wavevectors perpendicular to the imposed uniform magnetic field. Fluctuations present in the solar wind also display anisotropic behaviour [see, *e.g.*, *Horbury et al.*, 2011; *Matthaeus and Velli*, 2011], in the sense that various turbulence properties vary when considered at different angles relative to the average magnetic field [see, *e.g.*, *Weygand et al.*, 2011]. These observations will be discussed in greater detail below.

To take into account such wavevector anisotropies, several approaches are taken in modelling the turbulence in the solar wind, and hence the power spectra, based on assumptions as to the nature of the fluctuations, *viz.* the slab, 2D, and composite models [*Bieber et al.*, 1994; *Matthaeus et al.*, 1995; *Bieber et al.*, 1996; *Matthaeus et al.*, 2003]. Note that the so-called 'critical balance' theory of *Goldreich and Sridhar* [1995], although of relevance to the study of MHD turbulence [see, *e.g.*, *Forman et al.*, 2011], is beyond the scope of the present study.

In what follows, a right-handed coordinate system is used, with unit vector $\hat{\mathbf{z}}$ along $\mathbf{B}_o$, and spectra are described in terms of wavenumbers parallel ($k_{\parallel} = k_z$) and perpendicular (k_x, k_y) to $\hat{\mathbf{z}}$. Note that if the perpendicular fluctuations are assumed to be axisymmetric, the notation $k_{\perp} = \left(k_x^2 + k_y^2\right)^{1/2}$ will be used. The root mean square amplitudes of the fluctuations will be denoted by δB, with a subscript indicating the fluctuation type under consideration.

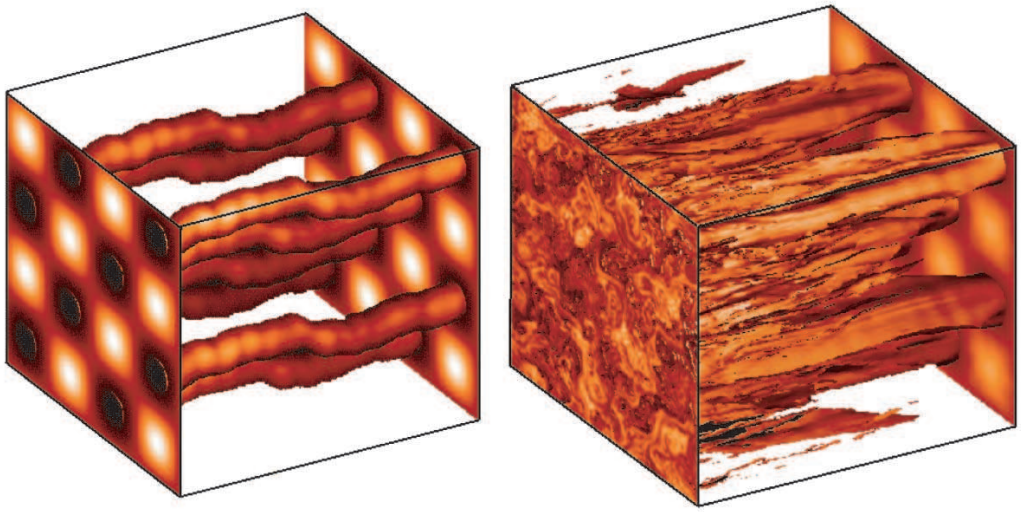

Figure 2.2: Magnetic flux tubes for pure slab turbulence (left panel) and $80/20$ composite turbulence (right panel) [*Matthaeus et al.*, 2003].

2.2.1 2D Turbulence

For the 2D model, fluctuations are assumed to be functions of transverse coordinates (x, y) only, such that the total magnetic field can be written as

$$\mathbf{B} = \mathbf{B}_o + \mathbf{b}(x, y) = B_o \mathbf{e}_z + b_{x,2D}(x, y)\mathbf{e}_x + b_{y,2D}(x, y)\mathbf{e}_y, \tag{2.10}$$

and the fluctuations are assumed perpendicular to the uniform component, so that $\mathbf{B}_o \cdot \mathbf{b} = 0$. The wavevectors associated with such fluctuations are assumed to remain on the (k_x, k_y) plane. Due to their divergence-free nature, the fluctuating component can be written in terms of some vector potential, defined by

$$\mathbf{b}(x, y) = \nabla \times a(x, y)\hat{\mathbf{z}}. \tag{2.11}$$

The function $a(x, y)$ is assumed to take a form so that no large spatial gradients are present, as such behaviour would violate the assumption of a uniform fluctuating component along z [*Ruffolo et al.*, 2004]. Fig. 2.3 illustrates such a potential function as an originator for two sets of field lines. Note that the field lines illustrated in this figure are not under the influence of purely 2D turbulence, but rather that of a composite slab-2D turbulence model, discussed below. For pure 2D turbulence, from Eq. 2.11 one would expect the varying magnetic field component $\mathbf{b}(x, y)$ to be perpendicular to $\nabla a(x, y)$, implying that a single field line would move along a line where $a(x, y)$ remains constant [*Ruffolo et al.*, 2004; *Chuychai et al.*, 2007]. A set of magnetic field lines starting out at the same value of z, but at different positions on the (x, y) plane, would each 'wander' differently, according to which 2D fluctuations (or, alternatively, which value of $a(x, y)$) they individually sample, following paths that are essentially independent as z increases [*Matthaeus et al.*, 1995]. This is illustrated in the bottom graphic of Fig. 2.4, where the initially well-defined magnetic surfaces on the far left of the image are completely shredded.

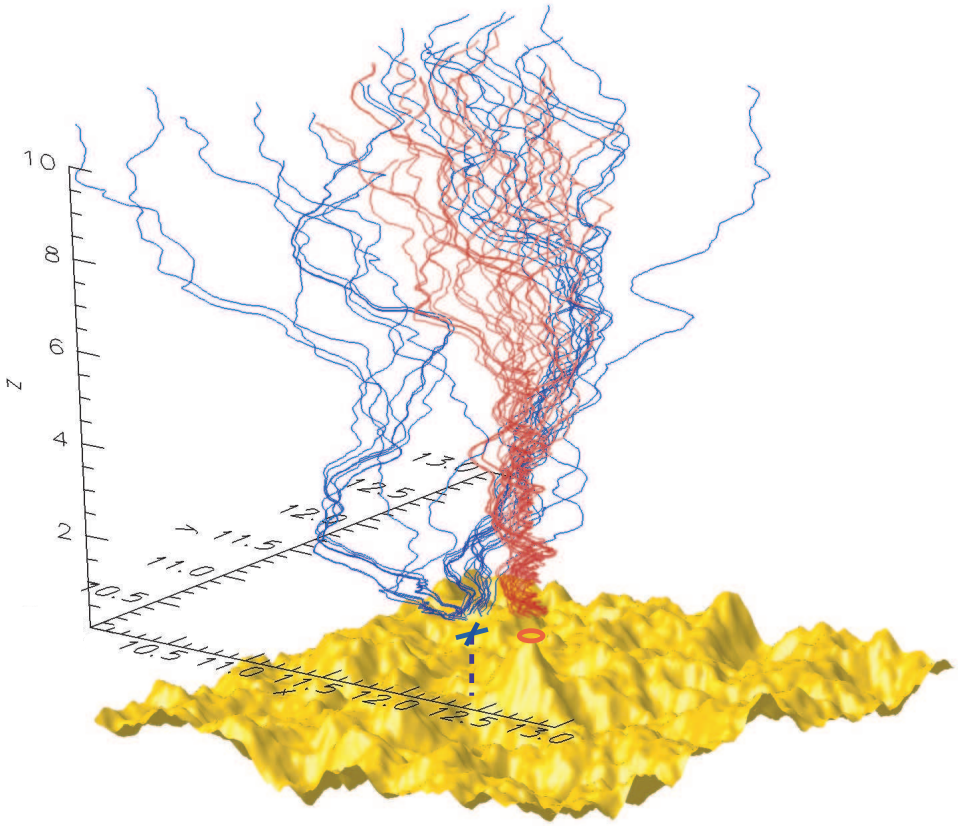

Figure 2.3: Two sets of simulated magnetic field line trajectories, starting at points of local minimum and maximum values of the potential function $a(x, y)$, X and O respectively, in the presence of composite turbulence. The yellow surface below represents the potential function $a(x, y)$ (see Eq. 2.11) corresponding to the 2D component of the turbulence [*Chuychai et al.*, 2007].

Assuming a large, finite box of length $2\pi L$, $a(x, y)$ can be expressed as a Fourier series within the box [*Matthaeus et al.*, 2007], *viz.*

$$a(x,y) = \sum_k \tilde{a}_L(k_x, k_y) \exp(i\mathbf{k}\cdot\mathbf{x}) \text{ with } k_x, k_y = 0; \pm k_o; \pm 2k_o \ldots \tag{2.12}$$

Here $k_o = 1/L$ is the smallest possible wavenumber within the box. Note that the periodic counterparts within the finite box of any variables here considered are denoted by a tilde. The homogeneous spectral density can then be found by extending the box to infinity independently of all other scales, so that [*Matthaeus et al.*, 2007]

$$\begin{aligned} A(\mathbf{k}) &= \lim_{L\to\infty} (L)^d \left\langle |\tilde{a}_L(\mathbf{k})|^2 \right\rangle \\ &= \lim_{L\to\infty} (L)^d \tilde{A}_L(\mathbf{k}), \end{aligned} \tag{2.13}$$

where for the 2D case, $d = 2$. Then, taking $\tilde{\mathbf{b}}_L = i\mathbf{k} \times \tilde{a}_L \hat{\mathbf{z}}$, one can write

$$\begin{aligned} S^L_{xx}(\mathbf{k}) &= \left\langle \left| \tilde{b}_x L(\mathbf{k}) \right|^2 \right\rangle = k_y^2 \tilde{A}_L(\mathbf{k}) \\ S^L_{yy}(\mathbf{k}) &= \left\langle \left| \tilde{b}_y L(\mathbf{k}) \right|^2 \right\rangle = k_x^2 \tilde{A}_L(\mathbf{k}), \end{aligned}$$

which correspond, in the infinite limit, to the homogeneous symmetric spectral tensor given in Eq. 2.4 with $S(\mathbf{k}) = k_\perp^2 A(\mathbf{k})$ and $A(\mathbf{k})$ the homogeneous spectral density. Although S_{ij}^{2D} is independent of k_z it can be embedded in a full three-dimensional spectrum by noting that

$$\begin{aligned} S_{ij}^{2D}(\mathbf{k}) &= \frac{1}{(2\pi)^3}\int_{-\infty}^{\infty} dx \int_{-\infty}^{\infty} dy \int_{-\infty}^{\infty} dz\, R_{ij}(x,y)\exp(-ik_x x - ik_y y - ik_z z) \\ &= \frac{\delta(k_z)}{(2\pi)^2}\iint_{-\infty}^{\infty} dx\, dy\, R_{ij}(x,y)\exp(-ik_x x - ik_y y) \\ &\equiv S_{ij}^{2D}(k_x,k_y)\delta(k_z). \end{aligned} \tag{2.14}$$

The total 2D turbulent energy (see Eq. 2.9) is given by

$$\begin{aligned} \int d^3k \left(S_{xx}^{2D}(\mathbf{k}) + S_{yy}^{2D}(\mathbf{k})\right) = \int d^3k S(\mathbf{k}) &= \iiint_{-\infty}^{\infty} d^3k (S_{xx}^{2D} + S_{yy}^{2D})\delta(k_z) \\ &= \iint_{-\infty}^{\infty} dk_x dk_y \left(S_{xx}^{2D} + S_{yy}^{2D}\right) \\ &\equiv \int_0^{\infty} 2\pi k_\perp dk_\perp \left(S_{xx}^{2D} + S_{yy}^{2D}\right) \\ &\equiv \int_0^{\infty} dk_\perp E^{2D}. \end{aligned} \tag{2.15}$$

The 2D omnidirectional energy spectrum E^{2D} is therefore related to the 2D modal spectrum by $E^{2D} = 2\pi k_\perp \left(S_{xx}^{2D} + S_{yy}^{2D}\right)$.

There are several lengthscales associated with the 2D spectrum, including the 2D ultrascale and the correlation length. The correlation length is related to the area under the correlation function such that R_{ij} assumes significantly non-zero values within this distance [*Choudhuri*, 1998], and hence can be interpreted as a characteristic lengthscale for the spatial decorrelation of the turbulent fluctuations [*Shalchi*, 2009]. The longitudinal and transverse correlation lengths, following *Matthaeus and Goldstein* [1982], can be defined generally as

$$\lambda_{c,j} = \frac{\int_0^{\infty} dr R_{jj}(r)}{R_{jj}(0)}, \tag{2.16}$$

where the subscript j denotes the Cartesian component involved in the direction of integration or one perpendicular to it. If axisymmetric 2D fluctuations are assumed, the total 2D correlation length is given by [*Matthaeus et al.*, 2007]

$$\lambda_{c,2D} = \frac{\int d^2k_\perp S^{2D}(k_\perp)/kk_\perp}{\delta B_{2D}^2}. \tag{2.17}$$

Matthaeus et al. [1999b] and *Matthaeus et al.* [2007] define a further lengthscale, the 2D ultrascale, relating it to the typical 'island' size of 2D turbulence, and which, again assuming axisymmetric fluctuations, can be expressed by

$$\lambda_{u,2D} = \sqrt{\frac{\int d^2k_\perp S^{2D}(k_\perp)/k_\perp^2}{\delta B_{2D}^2}}. \tag{2.18}$$

This quantity is interpreted by *Ruffolo et al.* [2004] as a lengthscale that is associated with the curvature of a correlation function, defined as in Eq. 2.2, but for the potential function $a(x,y)$, at zero separation.

If at the lowest wavenumbers the 2D spectrum is assumed to be flat down to zero wavenumber, Equations 2.17 and 2.18 yield diverging values. *Matthaeus et al.* [2007] discuss the wavenumber dependence when $k_\perp \to 0$, arguing that if the spectra and correlation functions were to be assumed homogeneous and analytic at the smallest values, finite energies are assumed, the fluctuations satisfy the solenoidal condition, and the spectrum were positive definite, the leading order behaviour of the modal energy spectrum can be expressed by

$$S^{2D}(k_\perp) = Ck_\perp^2 + O(k_\perp^4) \text{ as } k_\perp \to 0, \tag{2.19}$$

again assuming axisymmetric 2D fluctuations, and with C some constant pertaining to the level of the spectrum, more on which below. This, in effect, adds a new, 'inner' range to the discussion of the wavenumber dependence of the power spectrum in Section 2.1, implying the presence of a new, 'outer' scale separating this range from the energy range.

2.2.2 Slab turbulence

As proposed by *Jokipii* [1966], the slab turbulence model assumes that the fluctuating component of the total field is only a function of the coordinate z along which the uniform component is defined, *viz*.

$$\mathbf{B} = B_o\mathbf{e}_z + \mathrm{b}_{slab,x}(z)\mathbf{e}_x + \mathrm{b}_{slab,y}(z)\mathbf{e}_y, \tag{2.20}$$

where, if the fluctuations are assumed to be axisymmetric, $\mathrm{b}_{slab,x}(z) = \mathrm{b}_{slab,y}(z)$. Note that the fluctuating component is assumed perpendicular to the uniform component, so that the total magnetic field's lines do not track backwards for any z. The fluctuations are also assumed to propagate along $\hat{\mathbf{z}}$, and hence this model is used to describe Alfveń type fluctuations in the solar wind [*Goldstein et al.*, 1995a; *Osman and Horbury*, 2007]. A consequence of these assumptions is that a (uniform) field line experiencing purely slab turbulence will wander in (x, y) as z increases [see, *e.g.*, *Chuychai et al.*, 2007], however various field lines starting at different (x, y) coordinates but at the same z would wander in precisely the same way, as illustrated for magnetic flux tubes in the left panel of Figure 2.2, and in the top graphic of Fig. 2.4.

The assumption that the magnetic fluctuations in Fourier space are functions of the parallel wavenumber alone and that fluctuations in the two mutually perpendicular directions are uncorrelated, allows the spectral tensor to be written as

$$S_{ii}^{slab}(\mathbf{k}) = \left(\delta_{ii} - \frac{k_i k_i}{k^2}\right) S(k_z) = S(k_z). \tag{2.21}$$

Similar to the case for 2D turbulence, what now is a one-dimensional spectrum can be embed-

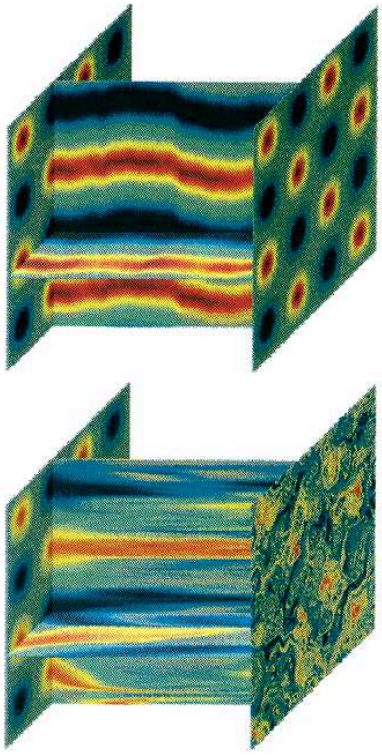

Figure 2.4: Simulated magnetic surfaces for slab (top) and purely 2D (bottom) turbulence [*Matthaeus et al.*, 1995].

ded in a full three-dimensional spectrum by noting that

$$\begin{aligned} S_{ii}^{slab}(\mathbf{k}) &= \frac{1}{(2\pi)^3}\int_{\infty}^{-\infty} dx \int_{\infty}^{-\infty} dy \int_{\infty}^{-\infty} dz R_{ii}(z) \exp\left(-ixk_x - iyk_y - izk_z\right) \\ &= \frac{\delta(k_x)\,\delta(k_y)}{2\pi}\int_{\infty}^{-\infty} dz R_{ii}(z) \exp\left(-izk_z\right) \\ &= S_{ii}^{slab}\delta(k_x)\,\delta(k_y) \\ &\equiv S_{ii}^{slab}\left(k_{\parallel}\right)\delta(k_{\perp}). \end{aligned} \tag{2.22}$$

The total slab turbulent energy is given by

$$\begin{aligned} \int dk^3 \left(S_{xx}^{slab}(\mathbf{k}) + S_{yy}^{slab}(\mathbf{k})\right) &= 2\int dk^3 S(\mathbf{k}) \\ &= \int\int\int_{\infty}^{-\infty} dk^3 \left(S_{xx}^{slab}(\mathbf{k}) + S_{yy}^{slab}(\mathbf{k})\right)\delta(k_x)\,\delta(k_y) \\ &= \int_{\infty}^{-\infty} dk_z \left(S_{xx}^{slab} + S_{yy}^{slab}\right) \\ &\equiv \int_{\infty}^{-\infty} dk_z E^{slab}, \end{aligned} \tag{2.23}$$

with E^{slab} the omnidirectional energy spectrum, which, for the slab case, is equal to the modal spectrum, $E^{slab} = S_{xx}^{slab} + S_{yy}^{slab}$. A lengthscale associated with the slab spectrum of interest to

the present study is the slab correlation length,

$$\begin{aligned}\lambda_{c,slab} &= \frac{\int dz R_{\perp}(z)}{\delta B^2_{slab}} \\ &= (2\pi)^2 \frac{\int_{\infty}^{-\infty} dk_{\parallel} G^{slab}\left(k_{\parallel}\right) \int_{\infty}^{-\infty} dz \exp\left(-izk_{\parallel}\right)}{\delta B^2_{slab}} \\ &= (2\pi)^2 \frac{\int_{\infty}^{-\infty} dk_{\parallel} G^{slab}\left(k_{\parallel}\right) \delta(k_{\parallel})}{\delta B^2_{slab}} \\ . &= (2\pi)^2 \frac{G^{slab}(0)}{\delta B^2_{slab}}, \end{aligned} \tag{2.24}$$

where $R_{\perp} = R_{xx} + R_{yy}$, and $G^{slab}(k_{\parallel})$ denoting the slab spectrum.

2.2.3 Composite turbulence

Often used to describe turbulence in the solar wind, the composite model represents a relatively simple superposition of fluctuations of the slab and 2D type, *viz.*

$$\mathbf{b}^{comp}(x, y, z) = \mathbf{b}^{slab}(z) + \mathbf{b}^{2D}(x, y). \tag{2.25}$$

Fig. 2.3 represents the trajectories of two magnetic field lines in the presence of such composite turbulence, while the right panel of Fig. 2.2 illustrates the behaviour of magnetic flux tubes subjected to composite turbulence, under the assumption that 80% of the total turbulent energy resides in the 2D fluctuations. From Fig. 2.3 it is clear that, due to the combination of the wandering of field lines in (x, y) as z increases caused by the slab component, and the fact that an extra fluctuating component that is solely a function of (x, y) is present due to the 2D component, the magnetic field lines exhibit a highly erratic behaviour. The composite model acts so as to braid and shred the flux tubes represented in Fig. 2.2, as opposed to the relatively well-behaved structure seen in the left panel of Fig. 2.2, where only slab turbulence was present. Note also that the coherent behaviour illustrated by the several flux tubes when only slab turbulence is considered, is no longer present when composite turbulence is assumed. Even though the flux tubes start at the same value of z, their initial (x, y)-coordinates are different, and thus the initial 2D component acting on each flux tube will be different.

The modal spectrum can be written as

$$S(\mathbf{k}) = S^{slab}(k_{\parallel})\delta(k_x)\delta(k_y) + S^{2D}(k_x, k_y)\delta(k_{\parallel}) = S^{slab}(k_{\parallel})\delta(k_{\perp}) + S^{2D}(k_{\perp})\delta(k_{\parallel}) \tag{2.26}$$

where, for the last step, axisymmetric 2D fluctuations are assumed. Again assuming such axisymmetry, the variance associated with composite turbulence can be expressed as

$$\delta B^2 = \delta B^2_{slab} + \delta B^2_{2D}. \tag{2.27}$$

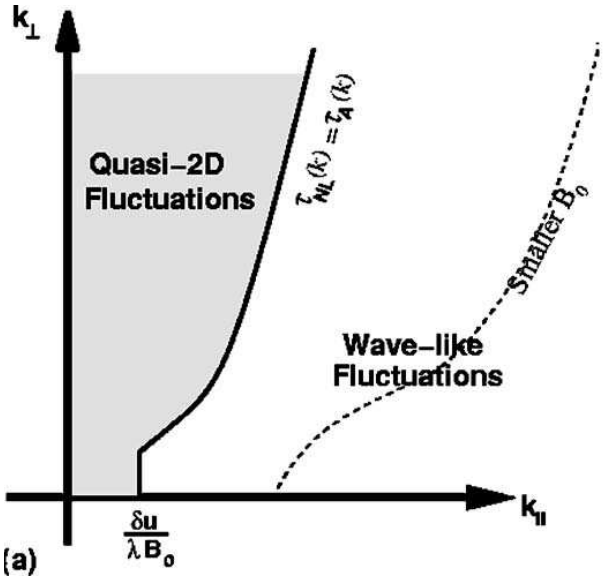

Figure 2.5: Quasi-2D and wavelike regions, with the boundary between them defined by $\tau_A(\mathbf{k}) = \tau_{nl}(\mathbf{k})$, in Fourier space [*Oughton et al.*, 2006]. Note that δu denotes the solar wind speed analogue to the magnetic variance, and λ a characteristic fluctuation lengthscale.

2.2.4 Quasi-2D and wavelike description

Oughton et al. [2004, 2006] present an alternative, yet related, way of describing MHD turbulence, in terms of a 'wavelike' component, where wave interactions dominate, and a 'quasi-2D' component, where nonlinear interactions hold sway. Given a fluctuating magnetic field component $\mathbf{b}$, the following two timescales can be defined as functions of the wavevector $\mathbf{k}$ associated with the Fourier transform of $\mathbf{b}$, respectively the Alfvén and nonlinear times, given by *Oughton et al.* [2004] as

$$\begin{aligned} \tau_A(\mathbf{k}) &= (\mathbf{k}\cdot\mathbf{B}_o)^{-1} = (k_\parallel B_o)^{-1} \\ \tau_{nl}(\mathbf{k}) &= (k\tilde{v}_k)^{-1} \approx (k\tilde{b}_k)^{-1}, \end{aligned} \tag{2.28}$$

where $k = |\mathbf{k}|$, and $\tilde{v}_k^2$ denotes the approximate energy per unit mass associated with the components of the Fourier transform of the fluctuating component $\mathbf{v}$ of the solar wind velocity. This quantity is approximately equal to its magnetic analogue $\tilde{b}_k$ should the uniform component of the Reynolds decomposition of the heliospheric magnetic field vector be stronger than the fluctuating component [*Oughton et al.*, 2004]. Note that magnetic fields are expressed in Alfvén speed units. For an extended discussion of these timescales, see also *Zhou et al.* [2004]; *Matthaeus et al.* [2012].

Two fluctuation components can be distinguished by considering the above timescales, in that wavelike fluctuations have, for a given wavenumber, a smaller Alfvén timescale than a nonlinear time scale. Similarly, fluctuations with a larger Alfvén time scale than their nonlinear timescale would be classified as quasi-2D, and would be relatively unaffected by parallel propagating fluctuations [*Oughton et al.*, 2006]. The low frequency component of the fluctuation

spectrum can be considered to be predominantly quasi-2D, while the higher frequency component is more wavelike [*Oughton et al.*, 2011]. The wavenumber at which $\tau_A(\mathbf{k}) = \tau_{nl}(\mathbf{k})$ separates the regions where either form of fluctuation dominates, and is a function of the strength of the assumed uniform component of the heliospheric magnetic field relative to the fluctuating component, as illustrated in Fig. 2.5.

The above prescriptions are sufficient to describe a fully 3D set of fluctuations, which incorporates the set of purely slab and 2D fluctuations described in the above Subsections [*Oughton et al.*, 2006]. Note that the quasi-2D component can be defined in a way similar to the 2D model discussed above, in that it allows for a fluctuating component parallel to the assumed uniform field which remains solely a function of transverse coordinates, so that [*Matthaeus et al.*, 2007]

$$\mathbf{b}^{2.5D} = (b_x(x,y), b_y(x,y), b_z(x,y)). \tag{2.29}$$

2.2.5 Reduced spectra

When measurements of turbulence quantities are taken by single spacecraft, only a time series is observed [see, *e.g.*, *Alexandrova et al.*, 2008; *Horbury et al.*, 2011]. As the solar wind is highly supersonic, and thus has a much larger velocity than the spacecraft, *Taylor* [1938]'s hypothesis can be made. A time series of data can then be converted into a one-dimensional spatial sample, in that fluctuations over a time scale t would correspond to fluctuations over a lengthscale rV_{sw} [*Osman and Horbury*, 2007; *Alexandrova et al.*, 2008; *Horbury et al.*, 2011]. When observations by single spacecraft of the correlation functions are considered, only measurements along a 'line' can be made, rendering it impossible to resolve the full three dimensional spectrum [*Matthaeus and Goldstein*, 1982; *Goldstein et al.*, 1995a; *Matthaeus et al.*, 2007; *Osman and Horbury*, 2007]. This limitation is effectively removed when multiple spacecraft observations are considered [see, *e.g.*, *Osman and Horbury*, 2007; *Weygand et al.*, 2009]. Therefore, what is usually observed by single spacecraft is the reduced power spectrum S^r_{ij}. If a spacecraft were to observe a correlation function $R(0,0,z)$ in, say, the z-direction, the reduced spectral tensor would be [*Matthaeus and Goldstein*, 1982]

$$\begin{aligned} S^r_{ij}(k_z) &= \frac{1}{2\pi}\int dz R_{ij}(0,0,z)\exp(-ik_z z) \\ &= \int\int dk_x dk_y S_{ij}(\mathbf{k})\,. \end{aligned} \tag{2.30}$$

Reduction of the spectrum implies no loss of information when purely slab turbulence is considered [*Matthaeus and Goldstein*, 1982], but in the presence of 2D turbulence, where $R_\perp = R_{xx} + R_{yy}$, there would be two independent reduced spectra, parallel and transverse, given respectively by [*Matthaeus et al.*, 2007]

$$S^r_{xx}(k_x) = \int_\infty^{-\infty} dk_y \left(1 - \frac{k_x^2}{k^2}\right) S(k_x,k_y) = \int_\infty^{-\infty} dk_y k_y^2 A(\mathbf{k}), \tag{2.31}$$

and

$$S^r_{yy}(k_x) = k_x^2 \int_\infty^{-\infty} dk_y A(\mathbf{k}). \tag{2.32}$$

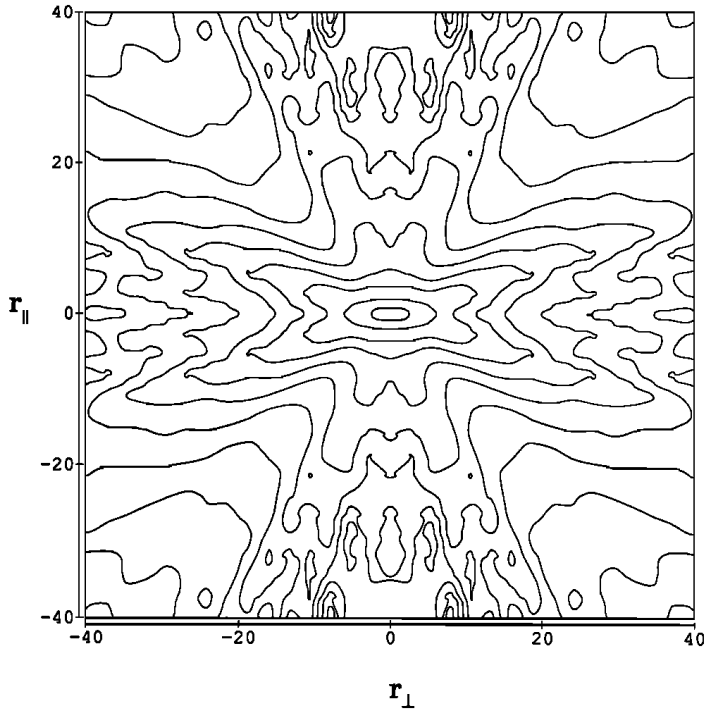

Figure 2.6: Contour plot of the 2D correlation function observed by [*Matthaeus et al.*, 1990]. Note that the axes are in units of 10^{10} cm, and that the plot was produced by reflecting the data from the top right quadrant.

If the 2D fluctuations are assumed axisymmetric, then $A(\mathbf{k}) = A[(k_x^2 + k_y^2)^{1/2}]$ and the above reduced spectra are no longer independent, but can be related by [*Matthaeus et al.*, 2007]

$$S_{yy}^r(k_x) = -k_x \frac{dS_{xx}^r(k_x)}{dk_x}. \tag{2.33}$$

As discussed by these authors, a consequence of this dependence is that if one spectrum becomes flat at small wavenumbers, the other one cannot be flat as well.

2.2.6 Dynamical turbulence

To include the effects of time-dependent decorrelation in the correlation function, and hence in models of solar wind turbulence, *Bieber and Matthaeus* [1991] and *Bieber et al.* [1994] propose a modification to the correlation function given in Eq. 2.2, so that the spectral tensor can be expressed by

$$S_{ij}(\mathbf{k}, t) = S_{ij}(\mathbf{k})\Gamma(\mathbf{k}, t), \tag{2.34}$$

where $S_{ij}(\mathbf{k})$ is the homogeneous spectral tensor defined in Eq. 2.4, and $\Gamma(\mathbf{k}, t)$ is known as the dynamical correlation function. *Bieber and Matthaeus* [1991] proposed that this function should scale as

$$\Gamma(\mathbf{k}, t) = \exp\left(-\alpha \left|\mathbf{k}\right| V_A t\right), \tag{2.35}$$

with V_A denoting the Alfvén speed, and $\alpha \in [0, 1]$ a parameter allowing for the adjustment of dynamical effects, $\alpha = 1$ implying strong dynamical effects, and $\alpha = 0$ the magnetostatic limit, with no dynamical effects whatsoever. This choice of Γ, known as the damping model of dynamical turbulence, allows for several physical timescales in the turbulence to be modelled. An example of this is that if α is interpreted as the ratio of the fluctuating to background magnetic fields, the timescale $\alpha |\mathbf{k}| V_A$ would correspond to the mean eddy turnover time [*Bieber et al.*, 1994], a timescale $\tau = l/u$ associated with a turbulent eddy with a characteristic length l and speed u [see, e.g., *Batchelor*, 1970]. *Bieber et al.* [1994] also argue that the exponential decay rate represented by the damping model could be taken to be equivalent to the Kolmogorov decay rate at the appropriate scales. Another model for dynamical turbulence, assuming a Gaussian correlation function, *viz*.

$$\Gamma(\mathbf{k}, t) = \exp\left(-\alpha^2 k^2 V_A^2 t^2\right), \tag{2.36}$$

is also proposed by *Bieber et al.* [1994], known as the random sweeping model for dynamical turbulence. Both of the abovementioned models have been extensively used to derive mean free paths from various scattering theories [see, e.g., *Bieber et al.*, 1994; *Teufel and Schlickeiser*, 2002, 2003; *Shalchi et al.*, 2006; *Shalchi*, 2009] and applied to the study of cosmic-ray modulation [see, e.g., *Burger et al.*, 2008; *Engelbrecht and Burger*, 2010].

2.3 Observations

A multitude of observations and simulations of solar wind turbulence have been made over the last decades, and this section can only attempt to list those believed to be most pertinent to this particular study. For greater detail and a broader perspective, the interested reader is referred to excellent reviews by, *e.g.*, *Goldstein et al.* [1995a], *Goldstein* [2001], *Bruno and Carbone* [2005], *Petrosyan et al.* [2010], *Horbury et al.* [2011], *Matthaeus and Velli* [2011], and *Matthaeus et al.* [2012]. Furthermore, in-depth expositions of the various methods and techniques employed in obtaining the observations discussed below are beyond the scope of this work, and again the interested reader is invited to consult the relevant references should more detail be required.

2.3.1 Wavevector and Power Anisotropy

Turbulence in the MHD regime has the distinct tendency to develop and sustain anisotropy relative to the direction of the large-scale magnetic field [see, e.g., *Shebalin et al.*, 1983; *Oughton et al.*, 1994; *Dasso et al.*, 2005]. Many such observations of wavevector anisotropy have been made over the past decades [see, e.g., *Matthaeus et al.*, 2012]. *Matthaeus et al.* [1990], investigating the 2D correlation functions using single spacecraft *ISEE* data, found evidence for fluctuations with wave vectors nearly transverse to both the mean magnetic field and the fluctuations about the mean. The two-dimensional correlation functions are shown in Fig. 2.6 in terms of distance parallel and perpendicular to the mean magnetic field, and exhibit a Maltese

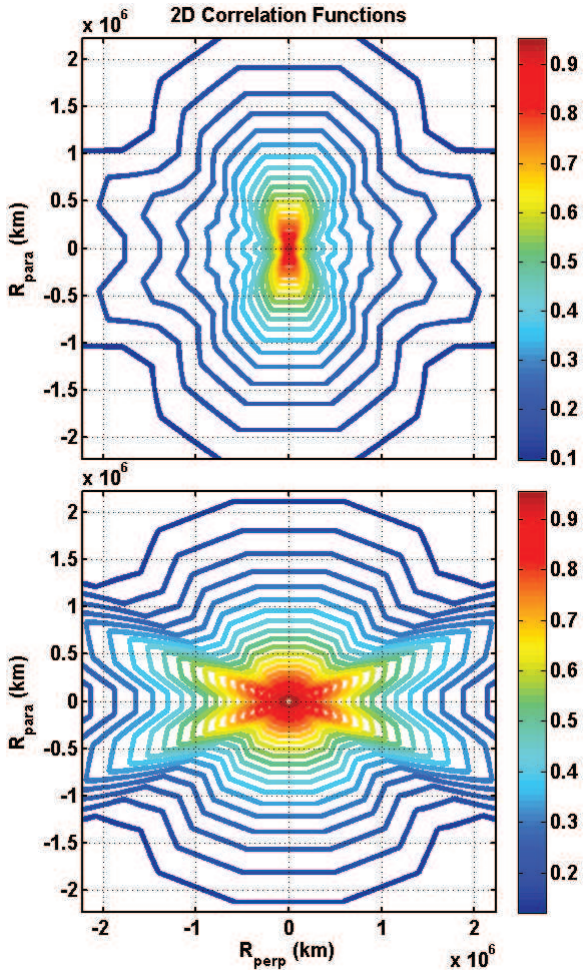

Figure 2.7: Contour plot of the 2D correlation function observed by *Weygand et al.* [2011] for the fast solar wind component in the ecliptic. The top figure represents contours the authors obtained from the sum of two exponential data fits, while the bottom figure represents results obtained from single exponential fits. For a detailed account of the analysis, see *Weygand et al.* [2011].

cross structure. The clear elongation of the structure perpendicular to the field (the horizontal 'beam' of the cross) indicates the presence of an Alfvénic, slab-like, component, while the elongation along the field indicates the presence of a two-dimensional component.

The analysis of *Matthaeus et al.* [1990] did not distinguish between fast and slow solar wind components. *Dasso et al.* [2005] performed such an analysis, considering fast and slow wind components at 1AU separately, and found evidence for wavevector anisotropies for both modes. These results, for the slow solar wind component, were in agreement with the findings of *Bieber et al.* [1996] in that a dominant 2D component was present. For the fast wind data, however, the authors found evidence for a slab dominated anisotropy. *Weygand et al.* [2011], analyzing data from multiple spacecraft in the ecliptic at ~ 1 AU comprised of contributions from regions of slow, intermediate, and fast solar wind speeds, consistently find anisotropies in the magnetic field fluctuations, such that fluctuations in the slow and intermediate wind are predominantly 2D. Figure 2.7 illustrates the correlation functions found by *Weygand et al.* [2011] for the fast so-

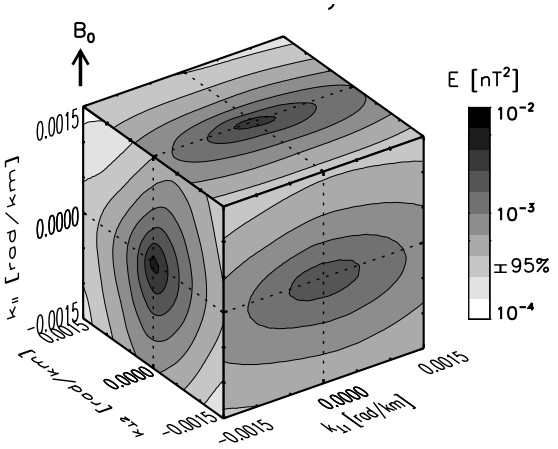

Figure 2.8: Cubic plot of the magnetic energy distribution for *Cluster* solar wind data, from *Narita et al.* [2010]. Note that a mean-field aligned coordinate system is used.

lar wind component. The correlation functions plotted therein show a fundamentally different structure to those of Fig. 2.6, indicating larger values of the correlation function perpendicular to the mean field, implying a slab dominated anisotropy. This is to some extent confirmed by the findings of *Perri and Balogh* [2010], who in an analysis of fluctuations observed by *Ulysses* in the fast solar wind, find that Alfvénic fluctuations predominate. Furthermore, *Bavassano et al.* [2000b] note that polar turbulence, at least at hourly scales, does not behave too differently from that seen for low-latitude fast solar wind streams. *Horbury et al.* [1995], in a variance analysis of inertial range fluctuations, find evidence that these fluctuations are highly anisotropic. Interestingly, a further study by *Wicks et al.* [2011] of fast solar wind fluctuations at 1 AU reports a scale dependence of the inertial range anisotropy, with the anisotropy decreasing with increasing spacecraft frequency. This raises the intriguing possibility of two distinct subranges within the inertial range of magnetic fluctuations. Lastly, *Wicks et al.* [2012] also find in a further, extensive analysis of *Ulysses* data evidence that the wavevectors in the fast solar wind beyond the ecliptic plane are anisotropic.

These analyses, however, were limited to observations taken by single spacecraft (see Subsection 2.2.5). Such observations are limited in the amount of information on the turbulence that they can resolve, and can also be confounded by the presence of intermittent high speed fluctuations, which render Taylor's hypothesis invalid [*Horbury et al.*, 2011]. Utilizing four-point *Cluster* data, *Narita et al.* [2010] were able to investigate the three-dimensional wavevector dependence of the solar wind magnetic fluctuations directly, without making use of Taylor's hypothesis, finding that the fluctuations were predominantly quasi-2D. This is illustrated in Fig. 2.8, which shows the magnetic energy distribution for a three-dimensional, mean field aligned, wavevector domain. *Osman and Horbury* [2007] also find evidence of anisotropic behaviour at inertial range scales, using *Cluster* data. Furthermore, again using *Cluster* data, *Narita et al.* [2011] find that this behaviour extends down to relatively small ($\sim$ 100 km) scales.

Due to observational constraints [see, e.g., *Horbury et al.*, 2011], measurements of the power

anisotropy of solar wind turbulence are difficult. Notwithstanding, *Bieber et al.* [1996] found that 2D fluctuations accounted for approximately 85% of the *total* inertial turbulent energy at 1 AU, the remaining $\sim 15\%$ belonging to slab fluctuations, a result confirmed by *MacBride et al.* [2010]. However, *Saur and Bieber* [1999], analysing 1 AU Omnitape data, find that $\sim 36\%$ of the total turbulent energy can be assigned to slab fluctuations, the remaining $\sim 64\%$ to 2D fluctuations. In the fast solar wind at high latitudes, *Smith* [2003] found from *Ulysses* data that approx. 50% of the energy could be assigned to 2D fluctuations, at ~ 4 AU. An observation at 1 AU by *Leamon et al.* [1998a], however, complicates matters somewhat, in that those authors, having found approx. 11% of the total turbulent energy in the inertial range to reside in slab fluctuations, found that this value increases to $\sim 46\%$ in the dissipation range, a result confirmed by *Hamilton et al.* [2008].

2.3.2 Symmetry of transverse fluctuations

In many studies of the anisotropy of solar wind fluctuations, the fluctuations themselves are assumed to be axisymmetric with respect to the mean field [*Horbury et al.*, 2011]. The first evidence for non-axisymmetry in magnetic field fluctuations was presented by *Belcher and Davis* [1971], who observed more power in fluctuations perpendicular to both the magnetic field and solar wind velocity than in any other direction, reporting a 5:4:1 anisotropy in fluctuations in terms of a field-aligned coordinate system defined by $(\mathbf{e}_B \times \mathbf{e}_r, \mathbf{e}_B \times (\mathbf{e}_B \times \mathbf{e}_r), \mathbf{e}_B)$, where $\mathbf{e}_B$ and $\mathbf{e}_r$ are respectively the field aligned and radial unit vectors. This observation has been confirmed by both *Narita et al.* [2010], and, to very small scales, by *Narita et al.* [2011]. However, *Turner et al.* [2011] argue that such observed non-axisymmetric properties may in fact be due to data sampling effects. These authors simulate axisymmetric fluctuations, and perform a virtual 'fly through' of the data, assuming Taylor's hypothesis to be true, and find that the fluctuations 'observed' exhibit non-axisymmetry. Furthermore, *Turner et al.* [2011] argue that data-sampling done utilizing techniques such as those used by *Narita et al.* [2010] could also in principle yield artificial asymmetries. That being said, it is interesting to note that *Wicks et al.* [2012] find, in an exhaustive study of *Ulysses* data, evidence of axisymmetry in polar turbulence.

2.3.3 Normalised cross-helicity and Alfvén ratio

Some controversy existed as to the nature of the fluctuations in the HMF, primarily as to whether they were turbulent in nature, as the findings of *Coleman* [1968] suggested, or whether they were primarily Alfvénic in nature, as reported by *Belcher and Davis* [1971]. *Matthaeus and Goldstein* [1982] aimed to address this issue by investigating the observed behaviour of various turbulence invariants, among which the cross helicity, defined as

$$H_c = \frac{1}{2} \int d^3x \mathbf{v} \cdot \mathbf{b}, \tag{2.37}$$

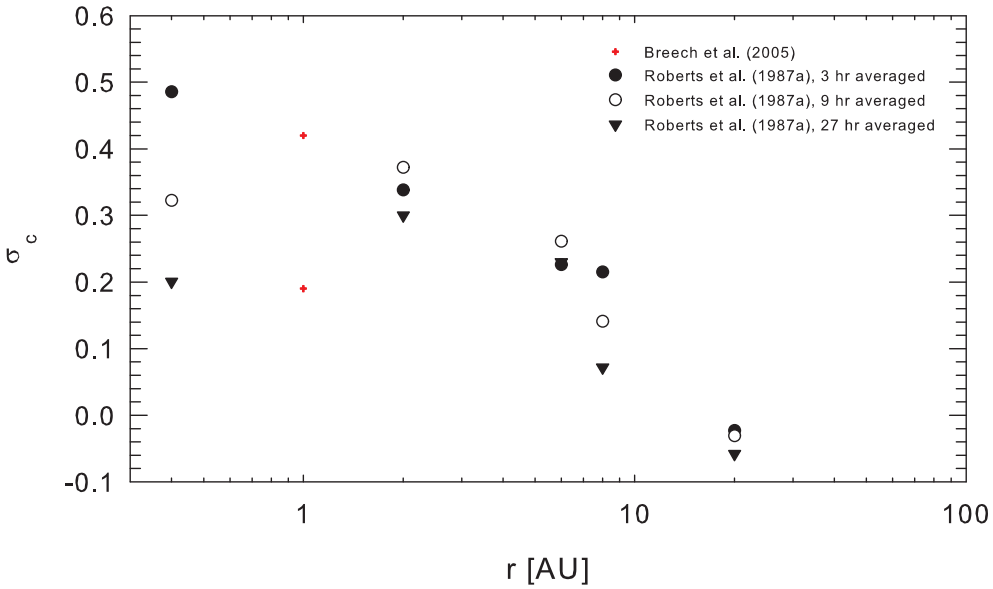

Figure 2.9: Normalised cross-helicities observed in the ecliptic, for various radial distances. Red crosses indicate values extracted by *Breech et al.* [2005] from *OMNI* data, while all other data represent values extracted from *Helios* and *Voyager* data by *Roberts et al.* [1987a].

where $\mathbf{v}$ denotes the fluctuating component of the solar wind velocity. The normalised cross helicity is defined so that it would assume a value of $+1$ if the fluctuations consisted only of Alfvén waves propagating outward from the sun. Any observed decrease in σ_c would be due to the presence of inward propagating waves [*Matthaeus and Goldstein*, 1982; *Roberts et al.*, 1987a, b; *Tu and Marsch*, 1993; *Goldstein et al.*, 1995a], with a value of -1 implying only inward propagating Alfvén waves. Furthermore, *Matthaeus and Goldstein* [1982] considered another quantity, the Alfvén ratio, defined as $r_A = E_v^r/E_b^r$, the ratio of the reduced velocity to magnetic fluctuation spectra. If the fluctuations were purely Alfvénic, this quantity would be observed to be equal to one [*Tu and Marsch*, 1993], while values less than unity would imply other kinds of possibly turbulent fluctuations. Numerical 2D incompressible MHD simulations have shown that shear instabilities in the solar wind could create inward propagating Alfvén waves (*Tu and Marsch* [1993], *and references therein*). *Matthaeus and Goldstein* [1982] found positive values for σ_c closer to the sun, with mixed positive and negative values at 5 AU, and values for the Alfvén ratio that varied between values of 0.8 and 0.4 for the inertial range of the power spectra considered. The further analyses of *Voyager* and *Helios* data performed by *Roberts et al.* [1987a] and *Roberts et al.* [1987b], the results of which are illustrated in Fig. 2.9 for various observation times, confirm these findings, in that the normalised cross helicity was found to decrease with increasing radial distance, implying some form of *in-situ* wave generation. Note that, from Fig. 2.9, the value of the calculated normalised cross helicity is quite sensitive to the observation time, as is clearly seen from the *Breech et al.* [2005] values, the larger of which is for spectra taken over a 24 hour period, the lesser for a 12 hour period. In a study of *ACE* data, *Milano et al.* [2004] find that σ_c is essentially isotropic with regards to the angle magnetic fluctu-

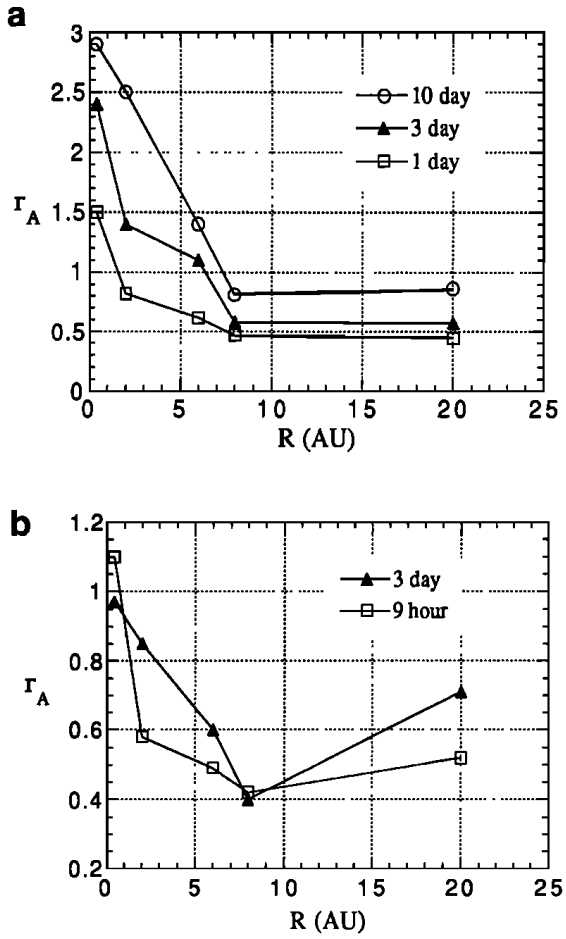

Figure 2.10: Alfveń ratios observed in the ecliptic by *Helios 2* and *Voyager 2*, reported by *Roberts et al.* [1990], for various averaging times. Panel (a) illustrates results acquired when the power in all three magnetic field components is taken into account, panel (b) when only non-radial components are taken into consideration.

ations have with respect to $\mathbf{B}_o$, implying some sort of interaction between the 'wave-like' and 'turbulence-like' components of the HMF described using the models discussed in Section 2.2. Furthermore, *Roberts et al.* [1987a, b] also investigated the behaviour of the Alfvén ratio, finding that this quantity has a value of ~ 1.0 at 0.3 AU, and decreases to a most probable value of ~ 0.5 beyond ~ 1 AU, a result confirmed by *Roberts et al.* [1990], and illustrated in Fig. 2.10. *Milano et al.* [2004] find that the normalised cross-helicity exhibits a rotational symmetry, in that it tends to be isotropic with regards to the angular distribution of the fluctuating magnetic field wavevectors. This, they conclude, implies a strong coupling between fluctuations considered to be two dimensional and those considered to be wavelike (see Subsection 2.2.4).

The Alfvén ratio also depends on the scale of the fluctuations, in that at the largest scales it approaches unity [*Matthaeus and Velli*, 2011], assuming the values discussed above at inertial scales [*Goldstein et al.*, 1995a; *Matthaeus and Velli*, 2011]. Within the inertial range of fluctuations itself, there is evidence of a further scale dependence, at least in the fast solar wind observed at Earth [*Wicks et al.*, 2011], shown along with the various spectra observed by these authors in Fig. 2.11, with values close to those reported above in the lower frequency range. Figure 2.11

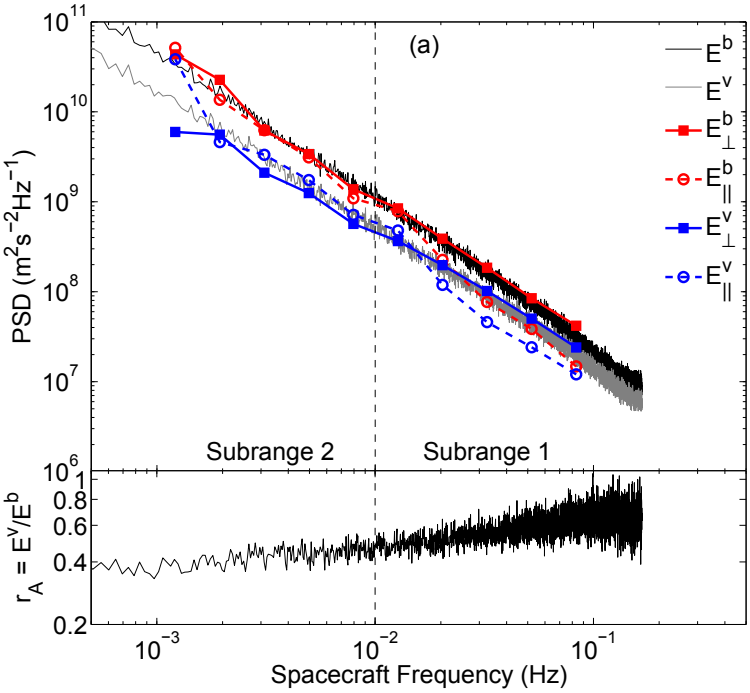

Figure 2.11: *WIND* power spectra (top panel) and Alfveń ratios (bottom panel) obtained by *Wicks et al.* [2011] for fast solar wind intervals at 1 AU.

also illustrates the extremely variable nature of the observed Alfveń ratio as observed in the solar wind.

The dominance of magnetic fluctuation energy implied by the observed less than unity values for r_A has been somewhat difficult to understand within the framework of MHD turbulence theory, with theories such as that of *Kraichnan* [1965] requiring an equipartition of fluctuation energies, and consequently an Alfveń ratio of one [see, *e.g.*, *Matthaeus and Goldstein*, 1982; *Tu and Marsch*, 1993]. However, the fluctuation transport model of *Tu and Marsch* [1993], incorporating two fluctuating components, *viz.* Alfveń waves and convective structures associated with small-scale variations that are perpendicular to the magnetic field, has been able to reproduce the Alfveń ratios and normalised cross helicities as observed in the ecliptic plane fairly well. MHD turbulence simulations can also account for this decrease in the Alfveń ratio, thereby solidly implicating the action, and presence, of turbulence in the solar wind [*Matthaeus and Velli*, 2011].

Figure 2.12 shows normalised cross helicities calculated by *Bavassano et al.* [2000a, b] using hourly averaged magnetic fluctuation energies taken during the first fast latitude scan (FLS) of *Ulysses*, as well as the corresponding latitude and radial position of that spacecraft as functions of time. These authors exclude observations about the ecliptic plane, as the emphasis of their study was on the behaviour of this quantity in the fast solar wind. The behaviour of the normalised cross helicity at the poles is interpreted by *Bavassano et al.* [2000b] as an indication of the greater Alfvénic component of polar turbulence, as opposed to that observed in the ecliptic

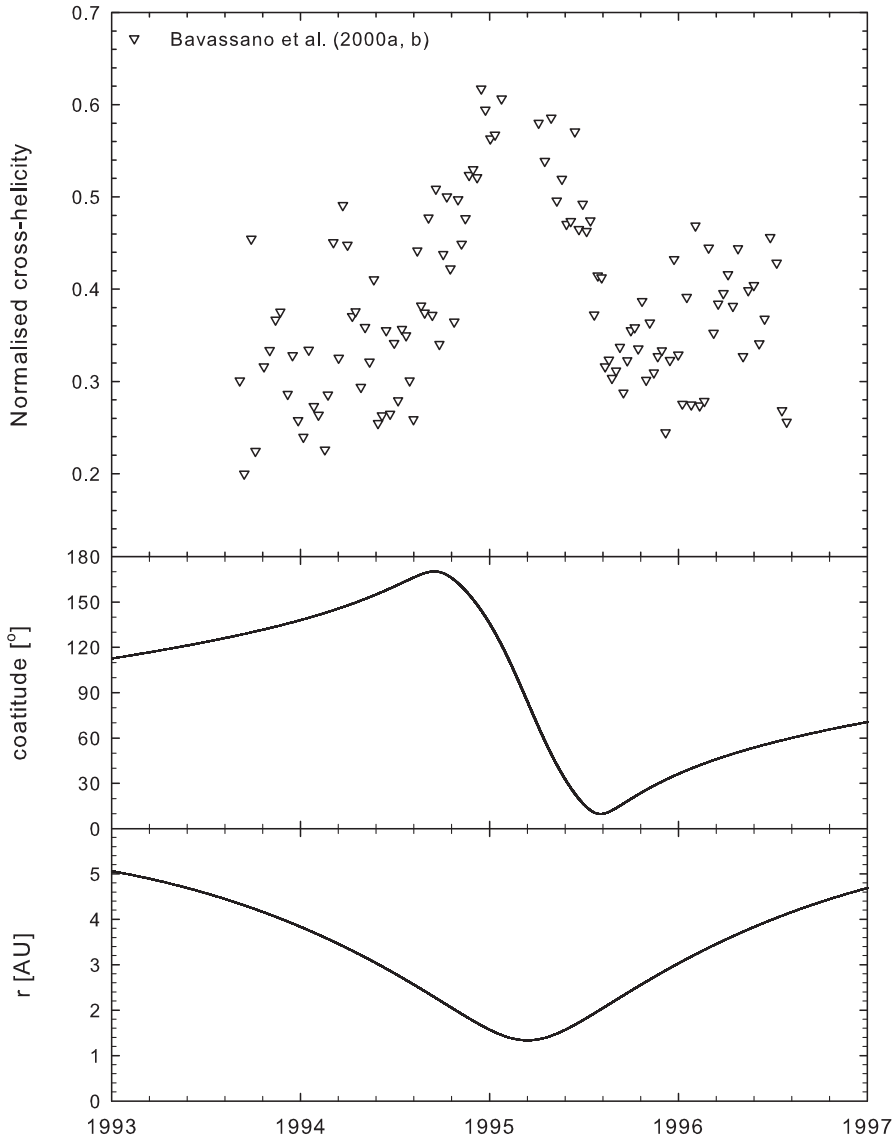

Figure 2.12: Normalised cross-helicities observed out of the ecliptic along the trajectory of *Ulysses*, reported by *Bavassano et al.* [2000a, b]. Note that all data points were taken for hourly averaged data. Spacecraft position as function of colatitude and heliocentric radial distance is illustrated in the bottom panels. Note the data gap spanning approximately $45°$ in latitude, centered on the ecliptic plane.

(see Subsection 2.3.1). These authors also find a decrease in the normalised cross helicity with increasing radial distance up to a distance of ~ 2 AU, reporting no further significant decrease beyond that. *Bavassano et al.* [2000b] also calculate a correlation coefficient for velocity and magnetic fluctuations, which decreases from a value close to unity at lower radial distances to a value of ~ 0.5 at ~ 2 AU, after which it remains on average approximately constant. The observed normalised cross-helicity, however, does tend to behave differently depending on which solar minimum is considered. During the solar minimum of solar cycle 22, the observed increase of σ_c during the first FLS performed by *Ulysses* was considerably steeper than that

observed during the solar minimum of solar cycle 23 [*Perri and Balogh*, 2010].

The observed systematic decrease of the normalised cross helicity cannot be explained within the framework of the Wentzel-Kramers-Brillouin (WKB) theory [see, *e.g.*, *Zank et al.*, 2012], which only concerns the propagation of MHD waves [see, *e.g.*, *Parker*, 1965b; *Barnes and Hollweg*, 1974; *Hollweg*, 1974; *Barnes*, 1992; *Matthaeus et al.*, 1994]. However, simulations and analytical models [see, *e.g.*, *Roberts et al.*, 1992; *Tu and Marsch*, 1993; *Oughton and Matthaeus*, 1995; *Breech et al.*, 2005, 2008; *Oughton et al.*, 2011] incorporating the effects of MHD turbulence can reproduce the observed decrease in σ_c, providing further evidence for a turbulent solar wind [*Matthaeus and Velli*, 2011].

2.3.4 Spectral Indices

Most observational results pertaining to the turbulent power spectra refer to either inertial range and dissipation range fluctuations, as data would typically have to be sampled for approx. 10 hours or longer to allow the energy range of the spectrum to be resolved [*Breech*, 2008]. Taking data over such long periods can lead to complications in its analysis, as, for example, the effects of intermittency of the interplanetary turbulence [*J.W. Bieber*, *private communication*, 2011]. Hence, for the energy range, some studies report a flat wavenumber dependence [*Hedgecock*, 1975], while others find a k^{-1} wavenumber dependence [*Marsch*, 1991; *Bieber et al.*, 1993; *Goldstein and Roberts*, 1999], as illustrated in Fig. 2.13. The k^{-1} wavenumber dependence may be due to the action of an inverse energy cascade [*Dmitruk and Matthaeus*, 2007]. Note that, at very low frequencies below the energy range, the displayed spectra exhibit a $f^{-1/3}$ dependence. This is due to the action of coherent structures in the solar wind, one example being approx. 27-day periodicities associated with solar rotation, and as such, the frequency dependence of this 'range' is highly variable [*Goldstein and Roberts*, 1999]. To further complicate matters, *Bieber et al.* [1993] report a solar cycle dependence of the energy range spectral index, with perpendicular and parallel magnetic spectra tending to be less steep, and having higher amplitudes, at periods of low solar activity. They also find that, at low wavenumbers, the energy range spectral indices for the perpendicular and parallel reduced spectra vary between -0.93 to -1.40 and -1.07 to -1.47, respectively, with steeper spectra corresponding to solar maxima. *Smith et al.* [1995], analyzing out-of-ecliptic *Ulysses* data, find that the spectrum flattens at the lowest frequencies, while *Horbury et al.* [1996] and *Goldstein et al.* [1995b] find a k^{-1} wavenumber dependence in their analysis. Furthermore, *Goldstein et al.* [1995b] consider spectra at 0.3 AU (*Helios* data), 2 AU (*Ulysses* data), and 4 AU (*Ulysses* data), and find that the spectral wavenumber dependence remains relatively unchanged as function of radial distance, in agreement with the earlier findings of *Bavassano et al.* [1982] for radial distances less than 1 AU.

Turning now to the inertial and dissipation ranges, *Coleman* [1968], obtaining magnetic power spectra at 1 AU, observed power law behaviours corresponding to the inertial and dissipation

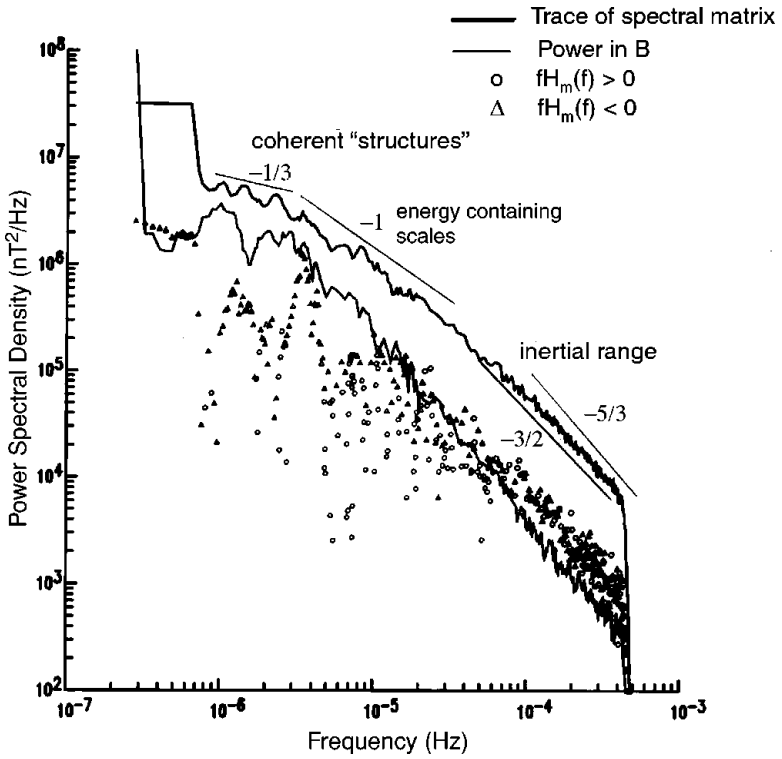

Figure 2.13: Magnetic power spectrum, representing data from a time series spanning more than a year, taken at 1 AU [*Goldstein and Roberts*, 1999].

subranges discussed in Section 2.1, find a spectral index of -1.2 for the inertial range. However, later studies found for the inertial range values for the spectral index close to both the Iroshnikov-Kraichnan and Kolmogorov values, with both sometimes within observational uncertainty [see, *e.g.*, *Matthaeus et al.*, 1982; *Tu and Marsch*, 1995; *Smith et al.*, 2006]. Figure 2.14 illustrates this well, showing the spread of spectral indices for the inertial and dissipation ranges observed by *Smith et al.* [2006], for both open magnetic structures and for magnetic clouds, at 1 AU. Out of the ecliptic, *Smith et al.* [1995] find inertial ranges with spectral indices corresponding to the Kolmogorov value. When out-of-ecliptic *Ulysses* data are considered, a Kolmogorov inertial range spectral index is observed [*Smith et al.*, 1995; *Goldstein et al.*, 1995b; *Horbury et al.*, 1996] at several radial distances [*Goldstein et al.*, 1995b]. *Chen et al.* [2011], in an analysis of *Cluster* inertial range intervals of data and numerical simulations, find that the inertial range spectral index is anisotropic with respect to the local mean field direction, with spectral indices for fluctuations with wavevectors perpendicular to the field exhibiting typically Kolmogorov values in the solar wind and Iroshnikov-Kraichnan values in simulations, these values gradually changing as wavevectors become more parallel to the local mean field vector to an inertial range scaling slightly steeper than k^{-2} for the solar wind data and exactly k^{-2} for simulations performed. The behaviour of the solar wind data corresponds to the predictions of the 'critical balance' theory of *Goldreich and Sridhar* [1995], and has been confirmed in further studies by *Osman and Horbury* [2009] and *Forman et al.* [2011]. The behaviour of

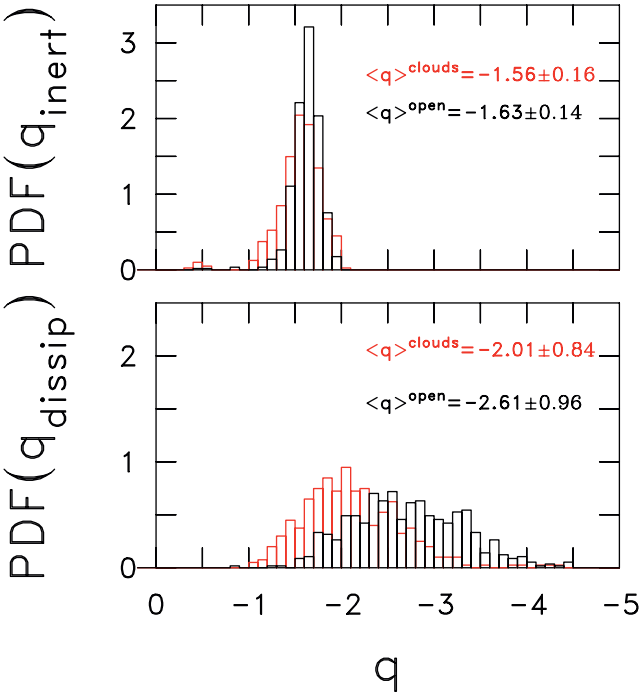

Figure 2.14: Distribution of the inertial range (top) and dissipation range (bottom) power-law indices (top) for open field lines and magnetic clouds at 1 AU [*Smith et al.*, 2006].

the simulations, however, has yet to be explained. These newer results show an obvious discrepancy with what has previously been found. *Chen et al.* [2011], however, argue that this is due to the fact that in their analysis they use the local mean magnetic field when considering anisotropies in fluctuations, as opposed to the global magnetic field used in prior studies. Interestingly enough, *Podesta* [2011] finds an inertial range spectral index for the perpendicular cascade at 1 AU corresponding to the Iroshnokov-Kraichnan $-3/2$ value.

In terms of the spectral evolution as function of increasing radial distance, *Roberts* [2010] investigated magnetic spectra from 0.3 AU to 5 AU, finding a consistently Kolmogorov-like inertial range, and conclude that such a spectrum would represent an asymptotic state for the turbulence in the magnetic field. *Roberts* [2010] also argues that the speed of the solar wind flow does not affect the inertial range spectral indices. *Goldstein* [2001] shows a fluctuation spectrum constructed from data taken at 10 AU by *Voyager 2*, which shows a $k^{-5/3}$ wavenumber dependence.

Given the discussion on dissipation range spectral indices in Section 2.1, the range of indices reported by *Smith et al.* [2006] (see Fig. 2.14) and *Hamilton et al.* [2008] (who find values for this quantity similar to those reported by *Smith et al.* [2006]) are difficult to reconcile with theory. As noted above, solar wind is a weakly collisional plasma, and hence descriptions of the behaviour of the turbulence in the dissipation range must of necessity be kinetic in nature. Various mechanisms have been proposed as to how dissipation occurs: *Stawicki et al.* [2001] proposed dispersion due to the action of whistler waves, while *Leamon et al.* [2000] argue that

the effects of Landau damping could also play a role. Ion cyclotron damping has also been proposed as a possible mechanism for turbulent dissipation [see, *e.g.*, *Goldstein et al.*, 1994]. This variety of possible mechanisms implies that the range of observed dissipation range should come as no surprise. Also, if dissipation were indeed to commence at wavenumbers corresponding to the ion inertial scale [*Leamon et al.*, 2000] (see Section 2.3.5), representing as it does the scale below which the fluid approximation breaks down [*Smith et al.*, 2006; *Alexandrova et al.*, 2008], the fact that the spectral index of the dissipation range depends on the rate at which energy cascades through the inertial range, as reported by *Smith et al.* [2006], should also play a role. *Smith et al.* [2006] conclude that if this were the case, and the lengthscale at which the dissipation range begins does not change, the form of the spectrum will adjust accordingly. It is intriguing to note, however, that *Alexandrova et al.* [2008] find evidence of a further inertial range beyond the abovementioned dissipation range onset lengthscale.

2.3.5 Lengthscales

The correlation length/correlation scale

The difficulties in resolving the energy range of the turbulence power spectrum (see Subsection 2.3.4) pertain equally to the observation of the lengthscale at which the inertial range commences, referred to in the present study as the 'turnover' scale. Observations of correlation lengths, or correlation scales, require only measurement of the correlation function (See Subsection 2.2.1), and thus are more readily available. This is not necessarily a problem when a turnover scale is required, as that quantity is often of the same order as the correlation length [*Weygand et al.*, 2011] and can in theory be calculated from a given correlation length, depending on the form assumed for the pertinent spectrum.

Bieber et al. [1994] combined survey results of *Hedgecock* [1975] and *Bieber et al.* [1993] at 1 AU, and found that a value of 0.03 AU for the slab correlation length allowed for a good fit of their chosen functional form for the slab spectrum. This result has been often used in theoretical and modulation studies involving cosmic-ray parallel mean free paths calculated from quasi-linear theory [see, e.g., *Teufel and Schlickeiser*, 2003; *Burger et al.*, 2008; *Engelbrecht and Burger*, 2010], and appears to be in fair agreement with the findings of subsequent investigations in the ecliptic plane described below. The 2D correlation length, however, has been assumed to be equal to one tenth of the slab correlation length [see, e.g., *Matthaeus et al.*, 2003], a factor that from more recent observations appears to be too small. *Weygand et al.* [2009], utilizing 1 AU data from nine different spacecraft in the ecliptic, find that the slab correlation length is 2.62 ± 0.79 times larger than the perpendicular correlation length in the solar wind, reporting values of 0.0374 ± 0.0107 AU and 0.0140 ± 0.0013 AU for those quantities, respectively. These authors, however, did not bin their observations according to solar wind speed. Using *ACE* data, *Dasso et al.* [2005] found that in slow solar wind streams at 1 AU the ratio of the parallel to perpendicular correlation lengths was ~ 1.18, while in the fast streams it assumed a value

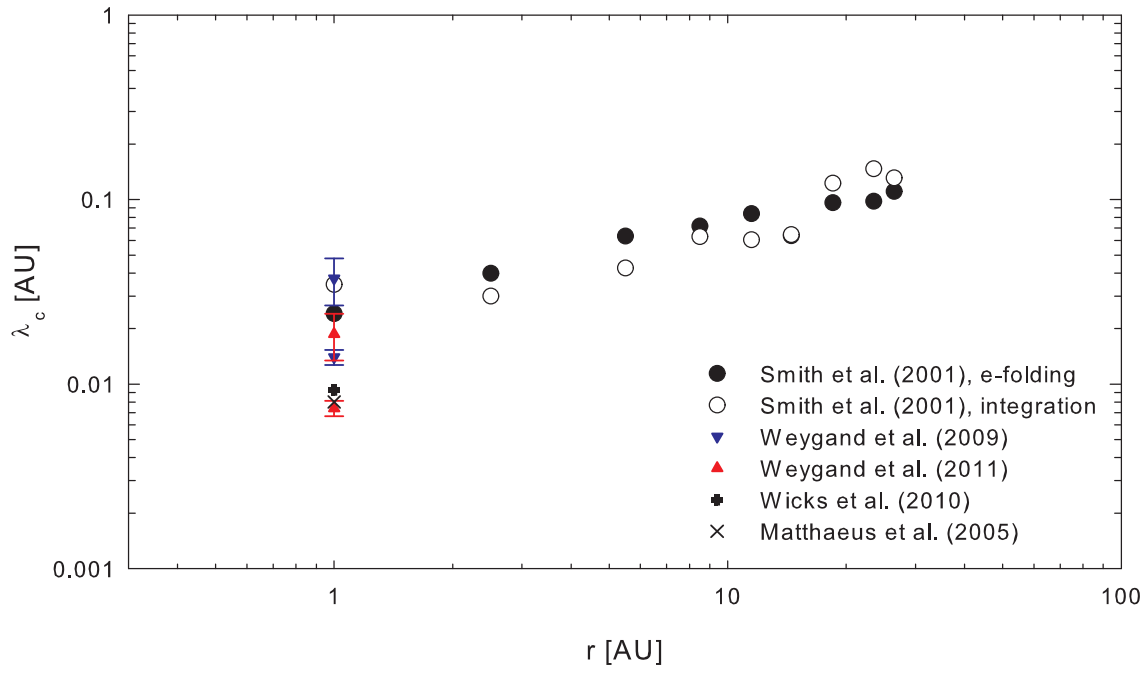

Figure 2.15: Correlation lengths observed in the ecliptic, for various radial distances. Black and white circles represent correlation scales computed with the e-folding and integration methods, respectively, from the N-component of Omnitape, *Pioneer 11*, and *Voyager 2* data [*Matthaeus et al.*, 1999a; *Smith et al.*, 2001], while the red symbols denote the results of *Weygand et al.* [2009], the larger of the two values corresponding to a correlation length for fluctuations nearly parallel to the mean field, the smaller to a correlation length for fluctuations most nearly perpendicular to the mean field. Blue symbols indicate observations by *Weygand et al.* [2011] for the slow solar wind component at 1 AU, the larger of the two values also corresponding to a correlation length for fluctuations nearly parallel to the mean field.The plus indicates a 35-year average value found by *Wicks et al.* [2010], while the 'x' below it represents the value found by *Matthaeus et al.* [2005].

Correlation length	Slow wind	Intermediate wind	Fast wind
Parallel	0.0187 ± 0.0053 AU	0.0187 ± 0.0007 AU	0.0067 ± 0.0013 AU
Perpendicular	0.0074 ± 0.0007 AU	0.0087 ± 0.0007 AU	0.0094 ± 0.0033 AU

Table 2.1: Values for the correlation length parallel and perpendicular to the mean magnetic field for different solar wind speeds at 1 AU, reported by *Weygand et al.* [2011]. Note that these values are plotted in both Figures 2.15 and 2.16.

of ~ 0.71. *Weygand et al.* [2011] also considered fast, intermediate, and slow solar wind components at 1 AU, but employed multiple spacecraft in their analyses, to some extent confirming the findings of *Dasso et al.* [2005]. These authors report that the observed ratio of the parallel to perpendicular correlation lengths differ for each solar wind speed mode they consider, assuming a value of 2.55 ± 0.76 for the slow component, 2.15 ± 0.18 for the intermediate, and 0.71 ± 0.29 for the fast component. Their findings as to the values of the respective correlation lengths are listed in Table 2.1. The implications of these results as to the anisotropy of the fluctuations is discussed in Section 2.3.1.

The picture at 1 AU in the ecliptic is, however, made more intriguing by the results of *Wicks et al.* [2009] and *Wicks et al.* [2010], who report, based on multiple spacecraft observations (span-

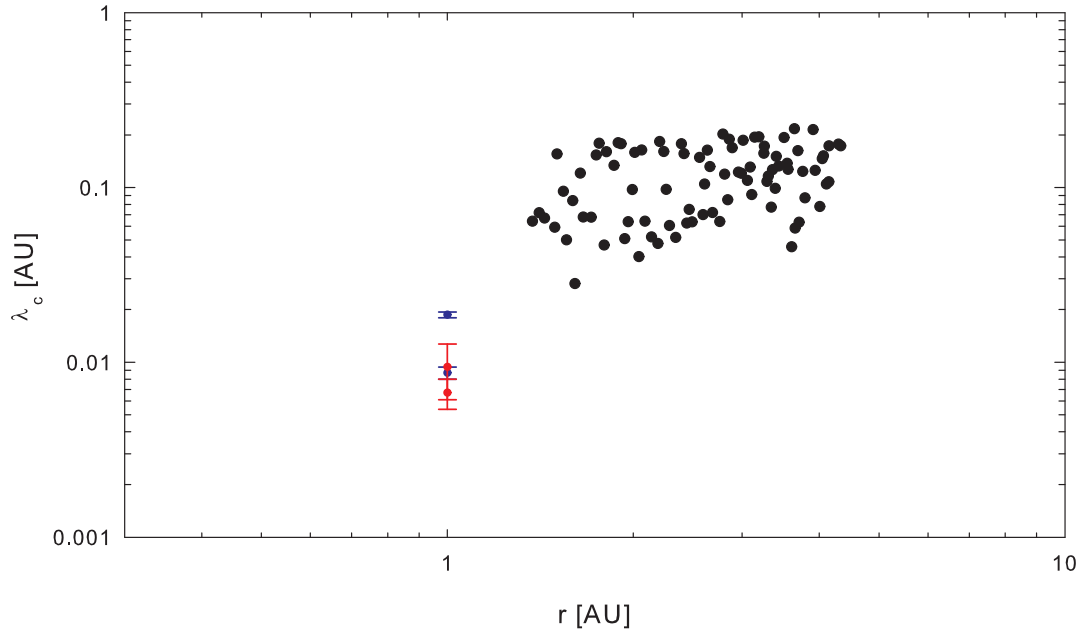

Figure 2.16: Correlation lengths observed out of the the ecliptic, for various radial distances. Black circles represent correlation scales at various radial distances *along the trajectory of Ulysses* during the first fast latitude scan, reported by *Bavassano et al.* [2000a, b]. The red and blue points respectively indicate values corresponding to fast and intermediate solar wind speeds observed at Earth by *Weygand et al.* [2011]. Note that the larger value of the red points corresponding to fast solar wind speed values represents the correlation length most nearly perpendicular to the mean magnetic field, while for the intermediate solar wind speed points the larger value corresponds to the correlation length parallel to the mean field.

ning ~ 35 years in the latter study), a solar cycle dependence of the correlation lengths. The values they observe during solar maxima are approximately twice those during solar minima, with *Wicks et al.* [2010] finding a 35-year average value for the total magnetic correlation length of 0.0093 AU. The observations discussed above are plotted in Fig. 2.15, including one of the first multiple-spacecraft observations of this quantity by *Matthaeus et al.* [2005], who report a value of 0.008 AU for the total magnetic correlation length. The solar cycle dependence of the correlation lengths adds another level of complexity to the process of choosing appropriate values of turbulence quantities as inputs for cosmic ray scattering theories and modulation studies.

Figure 2.15 also illustrates values for the correlation length associated with fluctuations in the N-component of *Voyager 2* and *Pioneer 11* data acquired by *Matthaeus et al.* [1999a] and *Smith et al.* [2001], calculated using two different techniques, the details of which can be found in *Smith et al.* [2001]. Beyond ~ 2 to 10 AU, these values can effectively be interpreted as corresponding to the 2D correlation length, as the heliospheric magnetic field here becomes almost perpendicular to the outward radial vector along which observations are taken, implying that single spacecraft would effectively observe a transverse reduced spectrum [*Zank et al.*, 1996; *Oughton et al.*, 2011]. The correlation length appears to be increasing relatively monotonically with radial distance, a result consistent with a picture of decaying turbulence in the outer he-

liosphere. Note that the spacecraft concerned had not yet left the ecliptic plane in a significant way when at the radial distances where these observations were being taken. In the light of the observations by *Wicks et al.* [2009] and *Wicks et al.* [2010], however, the times these observations were taken at relative to the solar activity cycle are of some significance, and correspond to a range of solar cycle conditions, spanning as it does the years 1973-1990 for *Pioneer 11*, and 1978-1989 for *Voyager 2*. As solar maximum conditions were prevalent for a large part of that period, it is possible that the 2D correlation length during solar minimum would be smaller than the observations by *Smith et al.* [2001]. Furthermore, *Matthaeus et al.* [2005] report that measurements of correlation lengths taken with single spacecraft are consistently 2-4 times larger than those taken utilizing multiple spacecraft.

Things become even less clear at higher latitudes. A large scatter of magnetic correlation length observations, taken by *Bavassano et al.* [2000a, b] utilizing *Ulysses* data taken during the first FLS, can be seen in Fig. 2.16. This is partly due to the large latitudinal excursion of the spacecraft during the period these observations were taken in, and any comparison with the observations of *Bavassano et al.* [2000a, b] must be taken along the trajectory of the *Ulysses* spacecraft. The scattering in the data is probably also due to the fact that during this excursion, the spacecraft sampled turbulence in fast, slow, and intermediate solar wind speed regimes. In the light of this, the fast and intermediate wind observations of *Weygand et al.* [2011] are included in Fig. 2.16, although they have been taken in the ecliptic plane. Note that the correlation lengths reported by *Bavassano et al.* [2000a, b] were observed during solar minimum conditions.

The dissipation range onset lengthscale

The smallest scale considered in this study is the break between the inertial range and the dissipation range of the slab spectrum. A value of ~ 0.44 Hz is reported for the dissipation range onset frequency at 1 AU by [*Leamon et al.*, 1998a], while *Hamilton et al.* [2008] report a value of ~ 0.3 Hz, and *Smith et al.* [2012] mention a value of ~ 0.2 Hz. Only two of the three models for the onset wavenumber of the dissipation range suggested by *Leamon et al.* [2000], those that give the best agreement with data, will be considered here. Those are where this lengthscale is either a function of the proton gyrofrequency [*Goldstein et al.*, 1994; *Leamon et al.*, 1998a], given by

$$\Omega_{ci} = |q_c| B_o / m, \tag{2.38}$$

where $|q_c|$ denotes charge and m mass, or of the local ion inertial scale ρ_{ii}, which can be expressed as

$$\rho_{ii} = \frac{V_A}{\Omega_{ci}}. \tag{2.39}$$

Leamon et al. [2000] argue that, should the latter be the case, the dissipation range would commence at the ion inertial scale due to the formation of local current sheet structures perpendicular to the mean magnetic field. These authors then compare these models to dissipation range onset wavenumbers they acquired from *Wind* data (the details of which analysis to be

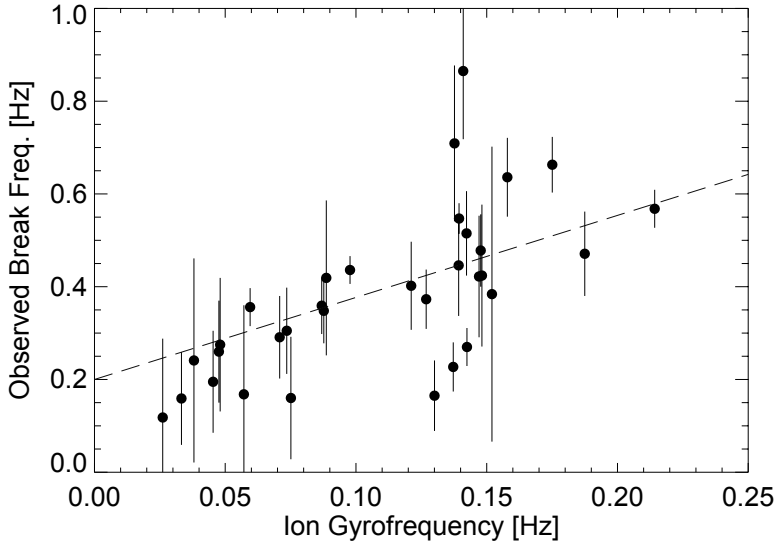

Figure 2.17: Observed spectral breakpoint frequency from 33 *Wind* intervals, as function of proton gyrofrequency. Dashed line indicates best fit regression [*Leamon et al.*, 2000].

found in *Leamon et al.* [1998b]), applying best-fit and fit through origin linear regressions to these observations, as illustrated in Figures 2.17 and 2.18, such that the dissipation range onset wavenumber can be expressed by

$$k_D = \frac{2\pi}{V_{sw}}(a + b\Omega_{ci}), \tag{2.40}$$

or

$$k_D = \frac{2\pi}{V_{sw}}(a + \frac{b}{2\pi}k_{ii}V_{sw}), \tag{2.41}$$

depending on the model chosen, with

$$k_{ii} = \frac{2\pi \sin\Psi}{\rho_{ii}} = \frac{2\pi\Omega_{ci}\sin\Psi}{V_A}, \tag{2.42}$$

and Ψ denoting the heliospheric magnetic field's winding angle. The regression constants a and b to be found in the above equations are listed in Table 2.2, given in terms of the dissipation range breakpoint frequencies associated with each model. As it turns out, the best fit proton gyrofrequency and best fit ion inertial scale models yield dissipation range breakpoint frequencies at 1 AU, listed in Table 2.3, closest to that observed by [*Leamon et al.*, 1998a], although the proton gyrofrequency models are in better agreement with the values given by *Hamilton et al.* [2008] and *Smith et al.* [2012]. However, the χ^2 value for the best fit ion inertial scale regression reported by *Leamon et al.* [2000] seems to imply that this model is most apt to describe the onset of the dissipation range, at least at 1 AU.

Outer scales

Various 'outer' scales that are larger than the above discussed correlation scale can be conceived of, especially for the case of two-dimensional turbulence, and related to the behaviour

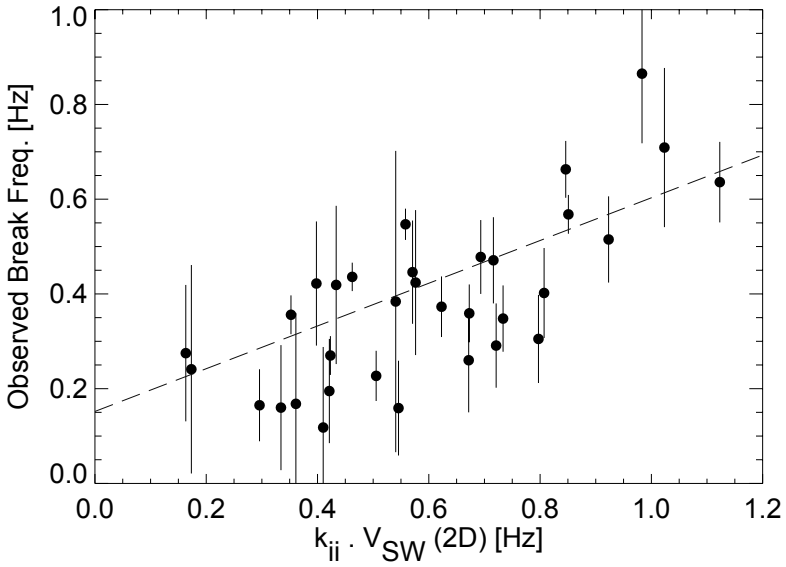

Figure 2.18: Observed spectral breakpoint frequency from 33 *Wind* intervals, as function of the Doppler-shifted wavenumber of perpendicular current sheet structures at the local ion inertial scale. Dashed line indicates best fit regression [*Leamon et al.*, 2000]. Note that the frequency $k_{ii}V_{sw}$ actually has units of radians per second and should be divided by a factor of 2π radians to give the units in Hz and the values given on the x-axis, as given in this figure from *Leamon et al.* [2000].

X	a	b	χ^2
$2\pi\Omega_{ci}$	0.200	1.760	2.93
	0	3.190	3.88
$k_{ii}V_{sw}$	0.152	0.451	2.66
	0	0.686	3.07

Table 2.2: Parameters and χ^2 values of regressions applied by *Leamon et al.* [2000] to observed breakpoint frequencies. Fits are of the form $\nu_{bp} = a + bX/2\pi$.

of the turbulence power spectrum at the smallest wavenumbers, if the turbulence were homogeneous [*Matthaeus et al.*, 1999b, 2007]. Their observation, however, is rendered very difficult by the limitations implicit to long-term observations of correlation functions discussed in the above subsections. One of these scales, the 2D ultrascale, so named due to its dependence on the behaviour of transverse fluctuations at very low wavenumbers, has been discussed in Subsection 2.2.1. *Matthaeus et al.* [1999b] argue that this ultrascale can potentially be related to the minimum lengthscale for which the 2D correlation function is equal to zero, and calculate such 'zero crossing' times from both sector-corrected *OMNI* data at 1 AU, and *Voyager 2* data. These observations, converted to lengthscales under the assumption of a 400 km/s solar wind speed, are illustrated in Fig. 2.19, alongside *Voyager* observations of the correlation scales discussed

$k_D(kii)$ Best fit	$k_D(kii)$ Through origin	Ω_{ci} Best fit	Ω_{ci} Through origin
0.452	0.456	0.298	0.178

Table 2.3: Values in Hz for the breakpoint frequency ν_{bp} at 1 AU predicted by the various models and fits of *Leamon et al.* [2000].

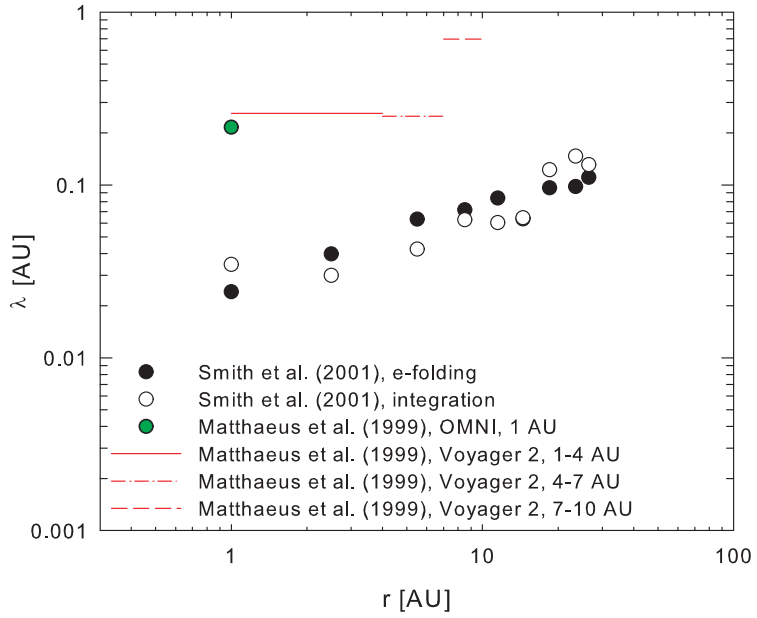

Figure 2.19: Zero crossing scales, as deduced from zero crossing times calculated by *Matthaeus et al.* [1999b] from *OMNI* and *Voyager 2* data. Correlation scales observed by *Smith et al.* [2001] are shown for comparison of magnitudes as the black and white circles.

above, to allow for some sort of a comparison of magnitudes.

Other potential outerscales include what *Matthaeus et al.* [1999b] call a 'MHD causality length', which would be the largest scale on which the turbulence at one point in the solar wind could influence the broader plasma, given local decorrelating effects such as the ongoing *in situ* MHD energy cascade, and the scale associated with the local breakdown of the assumption of homogeneous turbulence. This latter scale is estimated by *Matthaeus et al.* [1999b] to be of the the order of the radial heliocentric distance r, and to increase with radial distance. Another, related outer scale is that proposed by *Matthaeus et al.* [2007], which demarcates the boundary between the energy range in the 2D modal spectrum, and the theoretically expected power-law behaviour of the spectrum at the lowest wavenumbers (see Subsection 2.2.1).

Given the uncertainties of turbulence observations over such long timescales/low wavenumbers, and the difficulty of distinguishing between the abovementioned lengthscales therefrom, it yet remains unclear as to how these scales should properly be modelled. In what follows, the outerscale will therefore be considered to be essentially a free parameter, only bound by constraints like the assumption of a distinct energy range throughout the heliosphere.

2.3.6 Variances and fluctuation energies

The difficulties implicit to the observation of the turbulence quantities described above apply equally well to observations of the magnetic field variances and fluctuation energies. *Bieber et al.* [1994], in fitting a model power spectrum to the low wavenumber spectral observations of

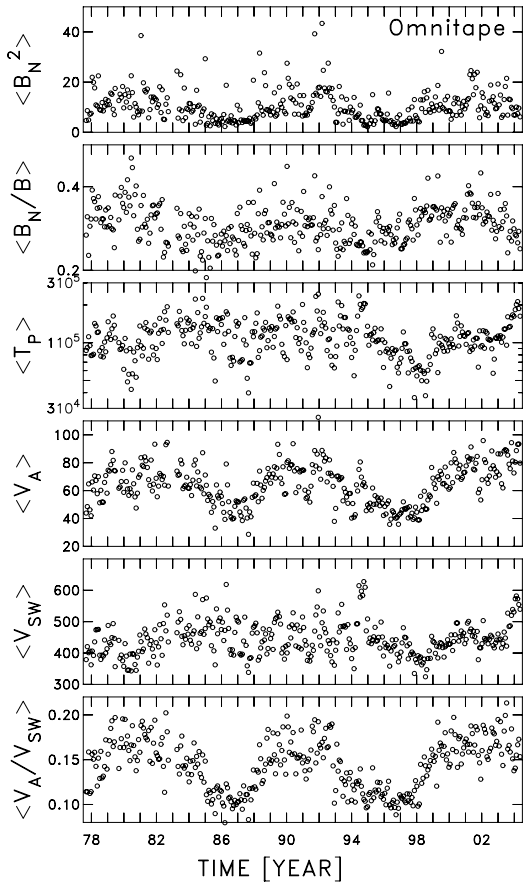

Figure 2.20: Solar wind parameters from the *OMNI* dataset, as function of time [*Smith et al.*, 2006b].

Hedgecock [1975] and *Bieber et al.* [1993], and to the inertial range spectral observations of *Wanner and Wibberenz* [1991], find a fit value of 13.2 nT^2 for the total variance of one perpendicular component of the heliospheric magnetic field, implying, with the assumption of axisymmetry, a value for the total variance at 1 AU of 26.4 nT^2. This value, however, requires some interpretation. Figure 2.20 illustrates observations of various solar wind parameters, as functions of time, and shows clear solar cycle dependences for each of the quantities considered. If the *Parker* [1958] model for the HMF is assumed at Earth (an assumption rendered relatively safe by the observations of, amongst many others, *Klein et al.* [1987]), it would follow that the mean meridional component of the observed background field would be zero, or negligible. Hence, any finite value observed for this quantity would be equal to half the total variance in the magnetic field, if axisymmetric fluctuations were assumed [*Smith et al.*, 2006b]. The top panel of Fig. 2.20 illustrates the square of the N-component of the magnetic field in the *OMNI* dataset, which corresponds to the theta component discussed above. During the two solar minima represented in the figure, an average value of ~ 6 nT^2 can be inferred, corresponding to a value of ~ 12 nT^2 for the total variance. On first impression, this value appears inconsistent with the findings of *Bieber et al.* [1994], but appears less so when it is noted that the spectral observations those authors used were taken during periods of ascending, and high, solar activity, which would imply, from Fig. 2.20, higher values for the magnetic variances. Some caution,

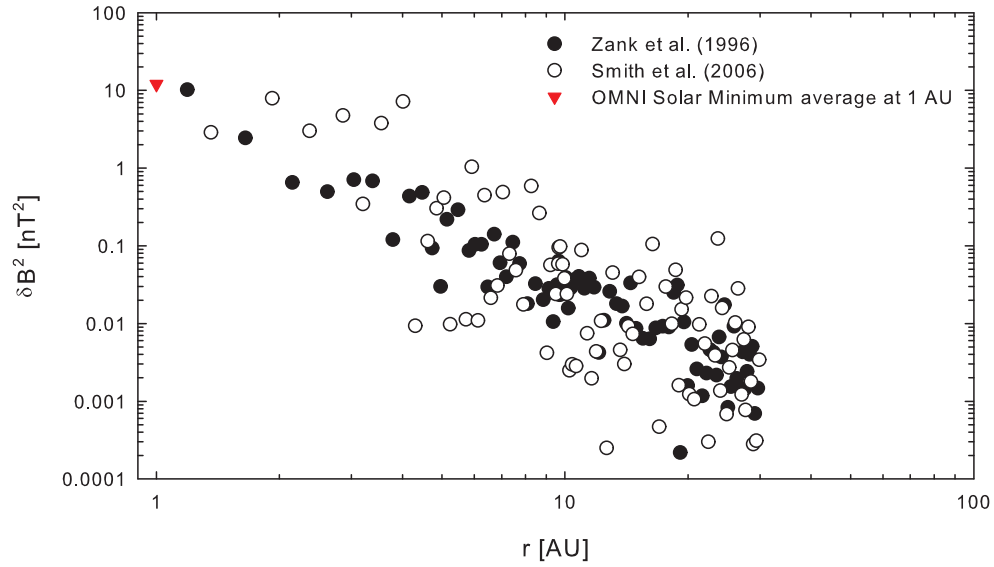

Figure 2.21: Total variances observed in the ecliptic, for various radial distances. Circles denote *Voyager 2* data reported by *Zank et al.* [1996] and *Smith et al.* [2006b] for the N-component of the observed magnetic field. Note that the abovementioned authors reported variances normalised to the magnetic field magnitude at Earth, while the above figure illustrates these data de-normalised, using a solar minimum value for the HMF magnitude at Earth of 5 nT^2, and that the total variance of 12 nT^2 is twice the value observed for the N-component of the HMF, following *Smith et al.* [2006b]. The red triangle denotes a solar minimum average value of the total variance calculated from OMNI data presented by *Smith et al.* [2006b].

however, has to be exercised in the interpretation and use of solar minimum variances. *Smith and Balogh* [2008] consider variances as observed at higher latitudes by Ulysses during the solar minima of solar cycles 22 and 23, finding a decrease of 25% in the total magnetic field variance observed during solar cycle 23, relative to that observed for solar cycle 22.

Figure 2.21 shows *Voyager 2* observations of the square of the N-component of the HMF reported by *Zank et al.* [1996] and *Smith et al.* [2006b], multiplied by a factor of two on the assumption of axisymmetry, as well as the ~ 12 nT^2 value at 1 AU discussed above. Note that the previous authors presented data normalised with values for the HMF magnitude taken at Earth, and as it is quite difficult to ascertain which precise values would be correct to de-normalise the data, this quantity being quite variable. Fig. 2.21 presents data that has been de-normalised using an average value of the HMF magnitude, during solar minimum, of 5 nT, commonly used in modulation studies [see, *e.g.*, *Jokipii*, 2001; *Ferreira et al.*, 2003; *Caballero-Lopez et al.*, 2004; *Caballero-Lopez et al.*, 2004a]. The data considered extends only to ~ 30 AU, as this is the radial extent to which *Voyager 2* remains roughly in the solar ecliptic plane.

The Wentzel-Kramers-Brillouin (WKB) theory, concerning as it does the transport of MHD waves only [see, *e.g.*, *Parker*, 1965b; *Barnes and Hollweg*, 1974; *Hollweg*, 1974; *Barnes*, 1992; *Matthaeus et al.*, 1994], predicts that the fluctuating component of the magnetic field would decrease in magnitude as $\sim r^{-3}$ [*Smith et al.*, 2001]. From Fig. 2.21, this is not entirely the case. In the

very inner heliosphere, within ~ 8 AU, the WKB theory provides a fair approximation to the radial dependence [see, *e.g.*, *Zank et al.*, 2012], but less so at larger radial distances, where the variance does not decrease as steeply. One possible explanation for this behaviour is that, outside of the ionization cavity, which extends to about 10 AU [*Vasyliunas and Siscoe*, 1976] (although values of 5.6 AU [*Oughton et al.*, 2011] and 8 AU [*Breech et al.*, 2008] have been used in various models) the formation of pickup ions from interstellar neutral hydrogen generates additional turbulence [*Lee and Ip*, 1987]. This mechanism has also been invoked to explain the non-adiabatic radial profile of the solar wind temperature observed by the *Voyager* spacecraft [see, *e.g.*, *Williams and Zank*, 1994; *Smith et al.*, 2001; *Smith et al.*, 2006b], discussed in more detail in Subsection 2.3.7. The data in Fig. 2.21, however, shows a fairly large amount of scatter, which could be due to a solar cycle dependence in the quantity concerned, and possibly partially due to the method of de-normalisation employed.

Bavassano et al. [2000a, b], in their investigation of normalised cross-helicities along the *Ulysses* trajectory, analysed the hourly inward and outward propagating magnetic fluctuation energies, denoted respectively by Z_+ and Z_-, and which are related to half the total fluctuation energy Z^2 by [see, *e.g.*, *Breech et al.*, 2005; *Minnie*, 2006; *Breech et al.*, 2008]

$$Z^2 = \frac{Z_+^2 + Z_-^2}{2}. \tag{2.43}$$

The magnetic variance in turn can be written in terms of Z^2, *viz*.

$$\delta B^2 = \frac{\mu_o \rho}{r_A + 1} Z^2, \tag{2.44}$$

with μ_o the permeability constant, ρ the solar wind mass density, and r_A the Alfveń ratio, discussed in Subsection 2.3.3. The *Bavassano et al.* [2000a, b] observations, shown in the top panel of Fig. 2.22, taken as they were during the first fast latitude scan, represent a sample of variances/fluctuation energies over a broad latitudinal range, as indicated by the middle panel of this figure. This quantity clearly has a complicated spatial dependence. Note that there is a gap in the data shown, extending about 45° centered on the ecliptic plane. Observations in this range were excluded by these authors due to their specific intention of studying turbulence at high latitudes. *Forsyth et al.* [1996] considered hourly magnetic variances as observed by *Ulysses*, reporting transverse variances larger in the polar regions than in the ecliptic, a finding later confirmed by *Erdös and Balogh* [2005] who argue that the latitudinal variation of the solar wind speed plays a significant role in the latitudinal variation of this quantity. *Forsyth et al.* [1996] also investigated the radial dependences of the hourly magnetic variances in the polar fast solar wind, and intriguingly enough, found that these dependencies did not agree with the predictions of WKB theory, a finding confirmed by both *Bavassano et al.* [2000a] and *Horbury and Balogh* [2001].

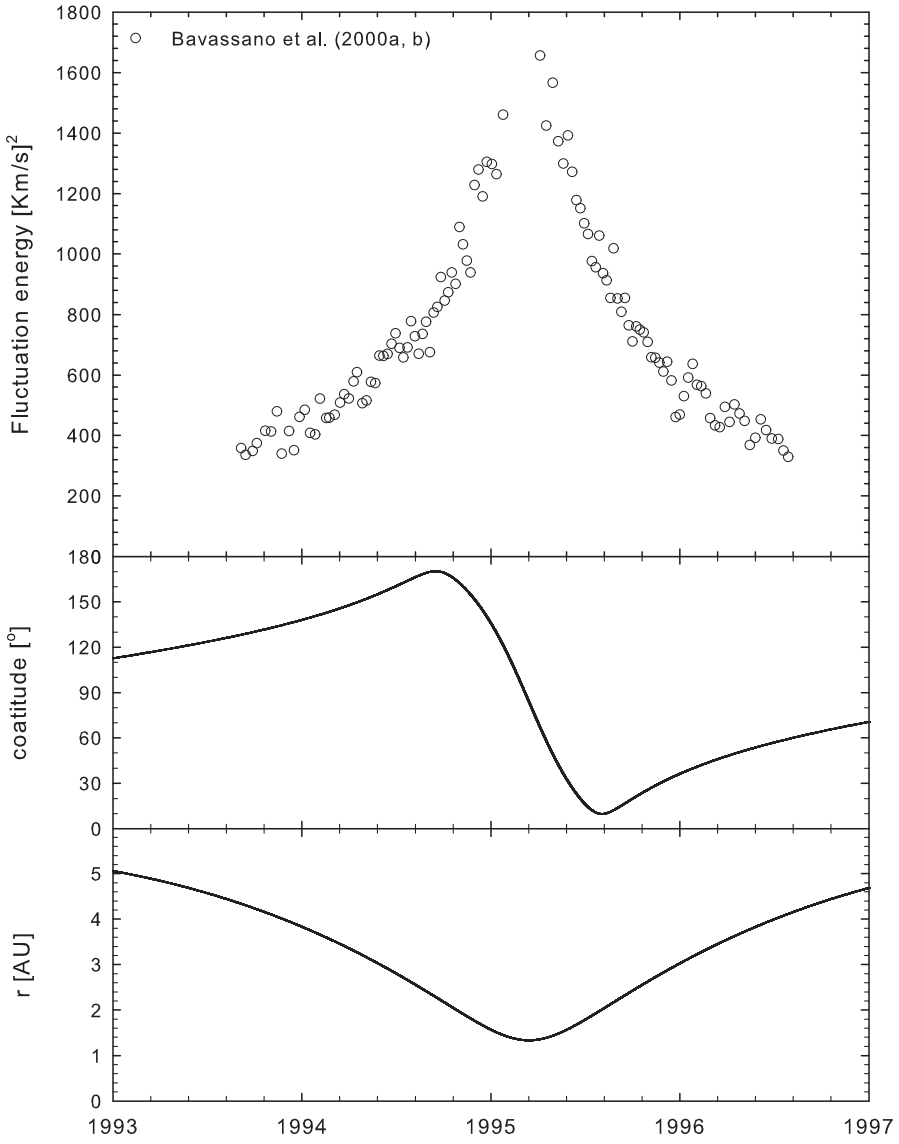

Figure 2.22: Total hourly fluctuation energy, acquired from *Ulysses* data by *Bavassano et al.* [2000a, b]. Bottom panels indicate the spacecraft's position when the observations were taken. Note the data gap spanning approximately $45°$ in latitude, centered on the ecliptic plane.

2.3.7 Solar wind temperature

One of the effects of a turbulent cascade is the deposition of energy into the background medium, thereby increasing its temperature [see, *e.g.*, *Davidson*, 2004]. Therefore the behaviour of the solar wind temperature can provide a diagnostic as to the effects of such cascade [*Williams and Zank*, 1994; *Williams et al.*, 1995; *Smith et al.*, 2001; *Isenberg et al.*, 2003; *Isenberg*, 2005; *Smith et al.*, 2006b; *Breech et al.*, 2009; *Isenberg et al.*, 2010].

Richardson et al. [1995], considering *IMP8* and *Voyager* solar wind proton temperature data, reported that the radial temperature profile deviated significantly from that expected from

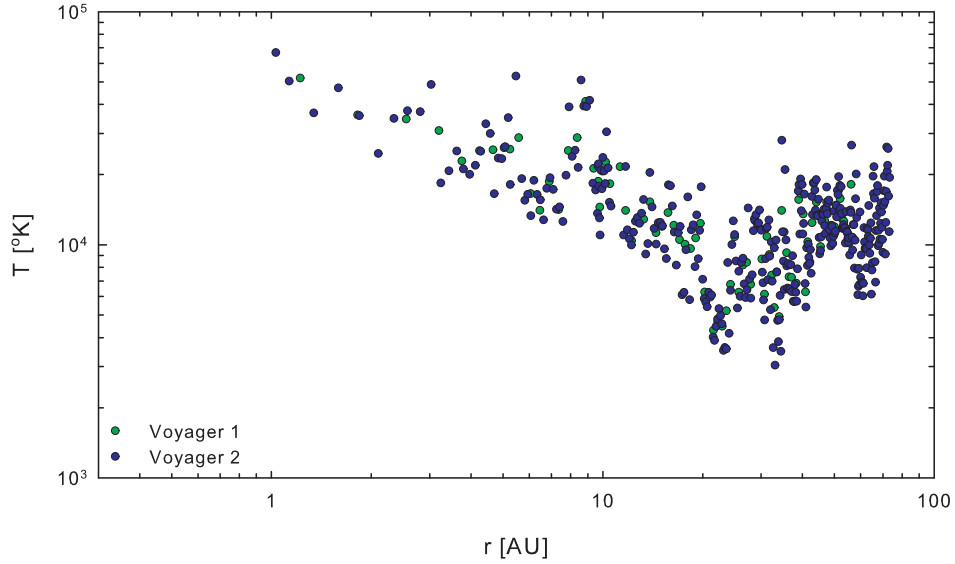

Figure 2.23: Solar wind proton temperatures observed along the trajectories of *Voyager 1* and *Voyager 2*, data from *Smith et al.* [2001].

purely adiabatic expansion, illustrated in Figure 2.23. Within approximately 10 AU, the $r^{-4/3}$ dependence expected from the adiabatic expansion of the solar wind can clearly be seen, beyond which the observed temperature decreases much more slowly with increasing radial distance, even increasing at the furthest radial distances, an effect which is not solar cycle related [*Smith et al.*, 2001]. One possible explanation proposed by *Richardson et al.* [1995] for the increase in temperature at the largest radial distances is that it is a latitudinal effect, as the *Voyager* spacecraft leave the ecliptic plane after $\sim 20-30$ AU. This explanation, however, does not explain the higher temperatures observed in the ecliptic. A possible source of energy for this phenomenon is the formation of pickup ions from interstellar neutral hydrogen, which could generate turbulence [*Lee and Ip*, 1987], the cascade of which would then deposit this energy as heat. As neutral hydrogen particles enter the heliosphere, they become ionized either by charge exchange mechanisms with solar wind protons [see, *e.g.*, *Zank*, 1999; *Fahr et al.*, 2000], or by solar ultraviolet light [see, *e.g.*, *Isenberg et al.*, 2003; *Isenberg*, 2005; *Breech et al.*, 2008]. This introduces an unstable distribution of pickup protons into the solar wind, which in turn are quickly scattered, generating wavemodes propagating parallel to the HMF [*Smith et al.*, 2001]. Only a fraction of the pickup ion's energy is deposited in this way [*Isenberg et al.*, 2003; *Isenberg*, 2005], but the energy contributed is significant enough to make this a viable heating mechanism [*Isenberg*, 2005]. Note that any turbulence transport model that includes only 2D-like fluctuations can therefore not include the effect of these pickup ions self-consistently.

To disentangle the combined radial and latitude dependence of the temperature along *Ulysses* trajectory as shown in Fig. 2.24 is not straightforward. *McComas et al.* [2000] report higher solar wind proton temperatures at higher latitudes. Figure 2.24 illustrates solar wind proton

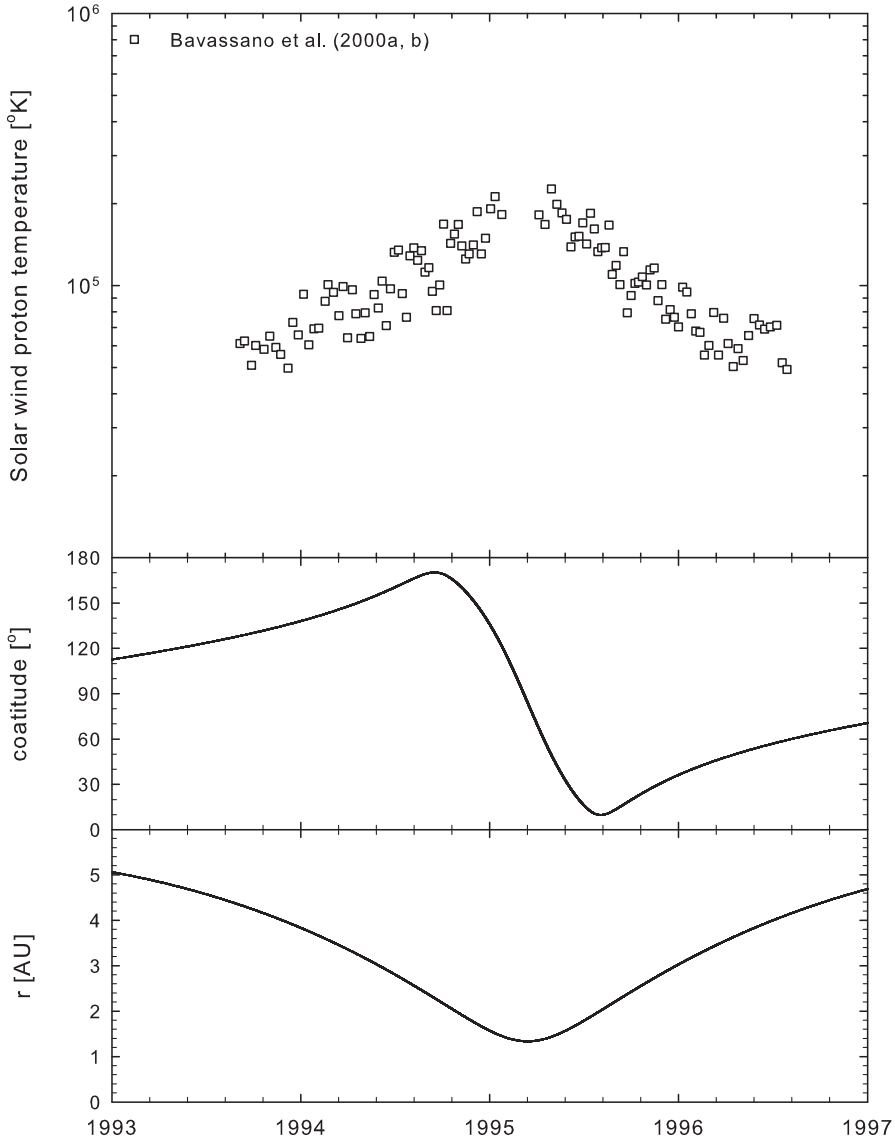

Figure 2.24: Solar wind proton temperatures observed out of the ecliptic along the trajectory of *Ulysses*, observed by *Bavassano et al.* [2000a, b]. Spacecraft position as function of colatitude and heliocentric radial distance is illustrated in the bottom panels. Note the data gap spanning approximately $45°$ in latitude, centered on the ecliptic plane.

temperatures, reported by *Bavassano et al.* [2000a, b], as observed by *Ulysses* during its first FLS. The proton temperatures continue to increase as the spacecraft moves towards the ecliptic, but it is also moving closer to the sun during this time. The solar wind temperature at 2 AU in the ecliptic can be seen from Fig. 2.23 to be ~ 35500 K, while at the same radial distance, but at a colatitude of $\sim 170°$, the temperature observed by *Ulysses* is significantly higher at ~ 135000 K. *McComas et al.* [2000] also report an r^{-1} radial dependence for the temperature (corrected for latitudinal effects), a finding close but not quite equal to, the expected adiabatic behaviour with exponent $-4/3$. Therefore the best approach to use when *Ulysses* data are employed as a

boundary condition, is to use this data along the spacecraft's actual trajectory.

2.4 Spectral models

Power spectra are key inputs in the scattering theories used to describe the diffusion of cosmic-rays in the heliosphere and therefore have a large role to play in cosmic-ray modulation [see, *e.g.*, *Shalchi et al.*, 2004c; *Shalchi*, 2009; *Shalchi et al.*, 2010b]. The following subsections will discuss and motivate choices made for the forms of the slab and 2D spectra later used to derive cosmic-ray diffusion coefficients. Note that each of the spectra discussed below are defined, in part, as functions of turbulence quantities such as the slab and 2D variances and spectral turnover scales. In the present study, the wavenumber dependences of the slab and 2D spectra are specified, and the turbulence quantities are modelled using a two-component turbulence transport model, which will be discussed in more detail in Section 3.2. Note that, throughout what follows, the assumption of axisymmetry will be made.

2.4.1 Model 2D spectrum

Observations indicate that a flat 2D energy spectrum, or one that goes as k^{-1} in the energy range may occur (see Section 2.3.4). Accurate measurements in this low-wavenumber regime are hard to come by, and the actual index may perhaps be something in between. A decrease at the lowest wavenumbers is however demanded by theory [*Matthaeus et al.*, 2007], and has to be incorporated. For simplicity, two different forms for the 2D spectra are assumed in the present study following *Matthaeus et al.* [2007]. Assuming a flat energy range for the omnidirectional energy spectrum, one can define a modal spectrum as

$$G_0^{2D}(k_\perp) = \frac{1}{2\pi k_\perp} C_o \lambda_{2D} \delta B_{2D}^2 \begin{cases} (\lambda_{out} k_\perp)^q & \text{for } |k_\perp| < 1/\lambda_{out}; \\ 1 & \text{for } 1/\lambda_{out} \leq |k_\perp| < 1/\lambda_{2D}; \\ (\lambda_{2D} k_\perp)^{-\nu} & \text{for } |k_\perp| \geq 1/\lambda_{2D}. \end{cases} \tag{2.45}$$

where, taking into account that $\int_0^\infty dk E^{2D}(k) = \delta B_{2D}^2$,

$$C_0 = \left[\left(1 + \frac{\lambda_{2D}}{\lambda_{out}} \left(\frac{1}{1+q} - 1 \right) + \frac{1}{\nu - 1} \right) \right]^{-1}, \tag{2.46}$$

with the 2D turnover scale, and the outer scale denoted by λ_{2D} and λ_{out}, respectively, while the inertial range spectral index is denoted by ν, here assumed to be $5/3$. Note that no dissipation range is here defined, as the emphasis of this work will be on the effects of the large scale/small wavenumber behaviour of the spectrum. If the omnidirectional energy spectrum is assumed to have a k^{-1} wavenumber dependence in its energy range, the corresponding modal spectrum can be written as

$$G_{-1}^{2D}(k_\perp) = \frac{1}{2\pi k_\perp} C_{-1} \lambda_{2D} \delta B_{2D}^2 \begin{cases} \frac{\lambda_{out}}{\lambda_{2D}} (\lambda_{out} k_\perp)^q & \text{for } |k_\perp| < 1/\lambda_{out}; \\ (\lambda_{2D} k_\perp)^{-1} & \text{for } 1/\lambda_{out} \leq |k_\perp| < 1/\lambda_{2D}; \\ (\lambda_{2D} k_\perp)^{-\nu} & \text{for } |k_\perp| \geq 1/\lambda_{2D}. \end{cases} \tag{2.47}$$

with

$$C_{-1} = \left[\left(\ln \left(\frac{\lambda_{out}}{\lambda_{2D}} \right) + \frac{1}{1+q} + \frac{1}{\nu - 1} \right) \right]^{-1}, \tag{2.48}$$

again following *Matthaeus et al.* [2007]. The various forms of such a spectrum are illustrated in Fig. 2.25.

For a 2D omnidirectional spectrum with a flat energy range, the application of Eq. 2.17 yields a correlation length given by

$$\lambda_{c,2D} = 3\frac{C_0}{q}\lambda_{2D}. \tag{2.49}$$

If this quantity were known from observations, the 2D turnover scale λ_{2D} could then simply be calculated from the above expression, depending, of course, on what is assumed for λ_{out}. Such a simple, tractable calculation is not possible for the case of 2D spectrum with an energy range displaying a k^{-1} wavenumber dependence, and therefore, throughout what follows, λ_{2D} is calculated using Eq. 2.49. Note that in the present study, q is assumed to be equal to 3, following *Matthaeus et al.* [2007].

Both of the above spectra are defined so as to decrease rapidly with decreasing k at the lowest wavenumbers, as discussed in Section 2.2.1, ensuring that finite ultrascales exist for each. This is in contrast to the spectral forms assumed by, *e.g.*, *Shalchi et al.* [2004a] in the derivation of perpendicular mean free paths. Hence, applying Equation 2.18, for the flat omnidirectional spectrum, the 2D ultrascale follows as

$$\lambda_{u,0} = \sqrt{C_0 \lambda_{2D} \left(\left(\frac{1}{q-1} + 1 \right) \lambda_{out} + \left(\frac{1}{1+\nu} - 1 \right) \lambda_{2D} \right)}, \tag{2.50}$$

while for the k^{-1} omnidirectional spectrum, it is

$$\lambda_{u,-1} = \sqrt{C_{-1} \lambda_{2D}^2 \left(\frac{1}{q-1} + \frac{1}{1+\nu} + \log \left[\frac{\lambda_{out}}{\lambda_{2D}} \right] \right)}. \tag{2.51}$$

The 2D spectral forms chosen for this study do not include a dissipation range. While this is not necessarily a reflection of the actual 2D spectrum, it is nevertheless an assumption made due to mathematical convenience, and also due to the fact that the diffusion coefficients perpendicular to the mean HMF of cosmic rays appear to be most sensitive to the wavenumber dependence of the energy range of the 2D spectrum [see, *e.g.*, *Shalchi et al.*, 2009; *Qin and Shalchi*, 2012]. Note that the spectral forms discussed above all include a well-defined energy range, in contrast to those forms assumed by *Pei et al.* [2010a].

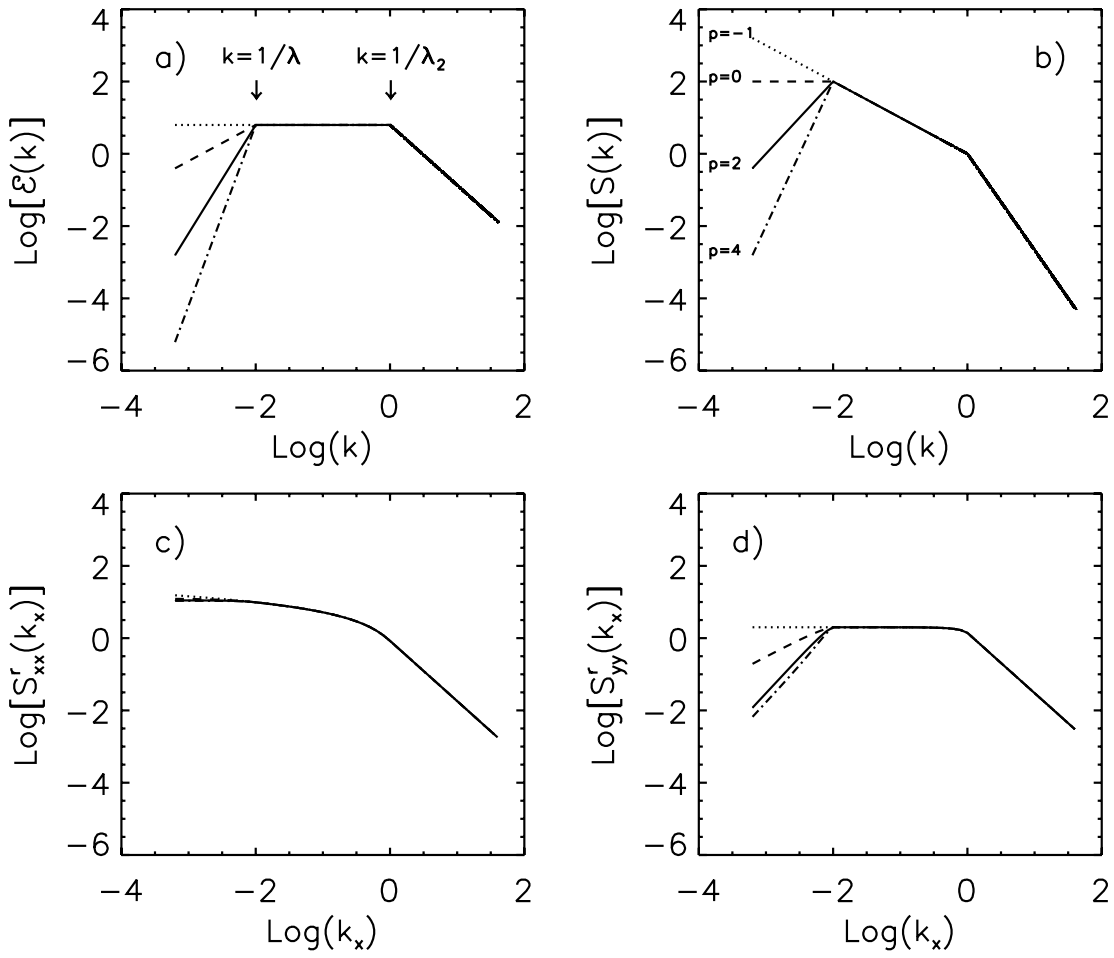

Figure 2.25: Various incarnations of an assumedly flat omnidirectional 2D spectrum, denoted in panel (a) by $\mathcal{E}$, from *Matthaeus et al.* [2007]. Panels (b) through (d) represent, respectively, the 2D modal, longitudinally reduced, and transverse reduced spectra, for various values of p, denoted by q in the present study. Note also that, in the present study, $\lambda_2 \equiv \lambda_{2D}$ and $\lambda \equiv \lambda_{out}$.

2.4.2 Model slab spectrum

The slab spectrum assumed in the present study, is that used by *Teufel and Schlickeiser* [2003], similar to the model of *Bieber et al.* [1994] and illustrated in Fig. 2.26, given by

$$G^{slab}(k_\parallel) \;=\; \begin{cases} g_o k_{min}^{-s} & \text{for } |k_\parallel| \le k_{min}; \\ g_o |k_\parallel|^{-s} & \text{for } k_{min} \le |k_\parallel| \le k_d; \\ g_1 |k_\parallel|^{-p} & \text{for } |k_\parallel| \ge k_d. \end{cases} \tag{2.52}$$

where $k_{min} = 1/\lambda_s$ is the parallel wavenumber associated with the slab turnover scale λ_s, and hence with the onset of the inertial range, and $k_d = 1/\lambda_d$ the wavenumber associated with the onset of the dissipation range. Furthermore, $g_1 = g_o k_d^{p-s}$, and

$$g_o = \frac{\delta B_{slab}^2 k_{min}^{s-1}(s-1)}{8\pi} \left[s + \frac{s-p}{p-1} \left(\frac{k_{min}}{k_d} \right)^{s-1} \right]^{-1}. \tag{2.53}$$

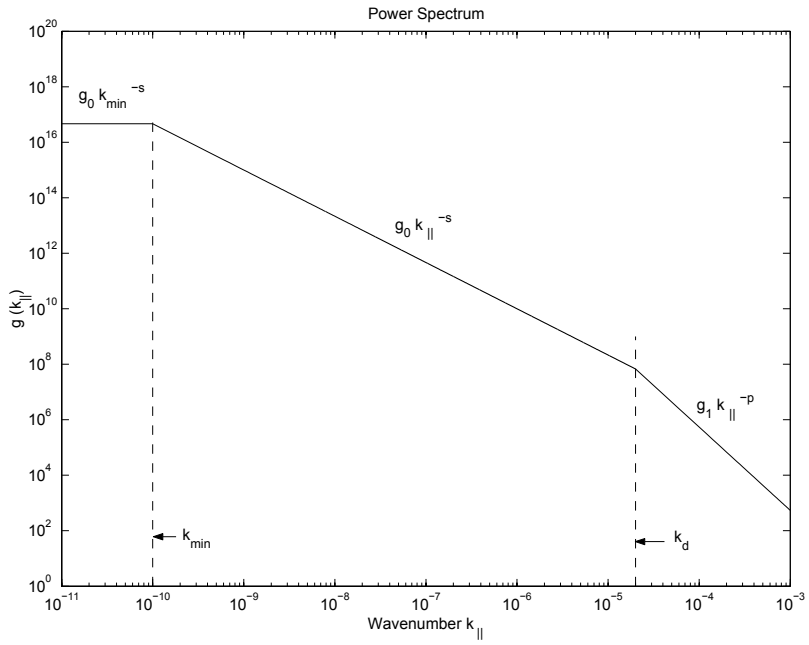

Figure 2.26: Slab turbulence power spectrum used in the present study, from *Teufel and Schlickeiser* [2003]. Note that the unit of $k_{||}$ in this figure is m^{-1}.

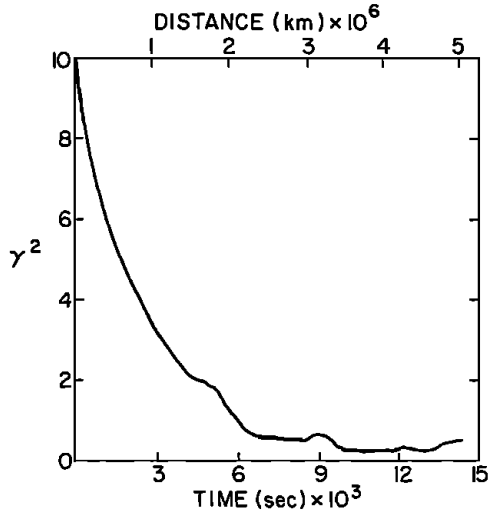

Figure 2.27: Magnetic field correlation function obtained by *Matthaeus and Goldstein* [1982] from 1 AU *Voyager 1* data. Note that the units of γ^2 are nT^2.

where the relation given in *Teufel and Schlickeiser* [2003] has been somewhat simplified. The spectral indices of the inertial and dissipation ranges are denoted respectively by s and p. These indices are here assumed to be equal to $5/3$ and 2.61 ± 0.96, following the findings of *Smith et al.* [2006]. This choice of inertial range spectral index is contradictory to the findings of *Osman and Horbury* [2009] and *Forman et al.* [2011], but is motivated by the fact that, when a spectrum with a Kolmogorov inertial range is used as an input for a parallel mean free path based on quasilinear theory, the rigidity dependence of such a mean free path is in agreement

with observations [see, *e.g.*, *Dröge*, 2000].

The slab correlation length can be calculated from Eq. 2.24 using Eq. 2.52:

$$\lambda_{c,slab} = \frac{\pi}{2} k_{min}^{-1} (s-1) \left[s + \frac{s-p}{p-1} \left(\frac{k_{min}}{k_d} \right)^{s-1} \right]^{-1}. \tag{2.54}$$

If an observed slab correlation length is given, the slab turnover scale $\lambda_s = k_{min}^{-1}$ can be calculated using Eq. 2.54, once it has been rendered tractable by means of the assumption $k_d \gg k_{min}$, which therefore 'hard-codes' the assumption of a well-defined inertial range throughout the heliosphere. Such a calculation yields

$$\lambda_s \approx \frac{5}{\pi} \lambda_{c,slab}, \tag{2.55}$$

in agreement with the result of *Matthaeus et al.* [2007] for a slab spectrum that consists only of a flat energy range, and a Kolmogorov inertial range.

This particular spectrum is constant at the lowest wavenumbers, and thus assumes a finite value at zero wavenumber. Even though this appears to be counterintuitive, in that it implies finite energies at infinite scales, the correlation function from which such a spectrum is constructed will asymptotically go to zero at large distance intervals [*Matthaeus et al.*, 2007]. Fig. 2.27 illustrates such a correlation function, obtained from 1 AU *Voyager 1* data by *Matthaeus and Goldstein* [1982].

The choice of dissipation range breakpoint wavenumber k_Ds can have large effects on cosmic-ray electron intensities [*Engelbrecht and Burger*, 2010]. The present study considers two of the models discussed by *Leamon et al.* [2000] for this quantity (see Subsection 2.3.5 for more background), the spatial variations of which being discussed in Subsection 4.5.1.

2.5 Summary

This concludes a brief introduction to such concepts in turbulence theory as are necessary to the self-consistent application of turbulence transport models to the study of the modulation of cosmic rays. This is necessitated by the fact that an adequate description of the diffusion coefficients for cosmic rays requires careful modelling of the cosmic ray mean free paths, which implies a choice of scattering theory. Realistic scattering theories require as an input a turbulence power spectrum [*Bieber et al.*, 1994; *Shalchi*, 2009], which in turn requires careful modelling of various turbulence quantities, such as the magnetic variance and correlation lengths. The results yielded by the turbulence models must then agree with such observations of turbulent quantities as have been made throughout the heliosphere and a brief review of these observations has been given. The choice of spectral forms is also important, in that it has a significant effect on the cosmic ray mean free paths. The model spectra chosen in the present study have also been discussed, and motivated observationally, as far as this is possible.

The following chapter will consist of an introduction to, and discussion of, the turbulence transport model used in this study, with a discussion of a set of boundary conditions for the model, chosen with the aim of reproducing as much of the available solar wind turbulence data as possible, both qualitatively and quantitatively.